Seasonal variability of the Ekman transport and pumping in the upwelling system off central-northern Chile (~30°S) based on a high-resolution atmospheric regional model (WRF)

Luis Bravo[1,2,3], Marcel Ramos[2,3,1,6], Orlando Astudillo[1,4], Boris Dewitte[4,3], Katerina Goubanova[5,4]

[1]Centro de Estudios Avanzado en Zonas Áridas (CEAZA), Coquimbo, Chile.
[2]Departamento de Biología, Facultad de Ciencias del Mar, Universidad Católica del Norte, Coquimbo, Chile.
[3]Millennium Nucleus for Ecology and Sustainable Management of Oceanic Islands (ESMOI), Coquimbo, Chile.
[4]Laboratoire d'Etudes en Géophysique et Océanographie Spatiales (LEGOS), Toulouse, France.
[5]Centre Européen de Recherche et de Formation Avancée en Calcul Scientifique (CERFACS), Toulouse, France.
[6]Centro de Innovación Acuícola Aquapacífico, Coquimbo, Chile

Corresponding author: luis.bravo@ucn.cl (L. Bravo), marcel.ramos@ucn.cl (M. Ramos)

Abstract

Two physical mechanisms can contribute to coastal upwelling in eastern boundary current systems, offshore Ekman transport due to the predominant along-shore wind stress and Ekman pumping due to the cyclonic wind stress curl, mainly caused by the abrupt decrease in wind stress (drop-off) in a cross-shore band of 100 km. This wind drop-off is thought to be an ubiquitous feature in coastal upwelling systems and to regulate the relative contribution of both mechanisms. It has been poorly studied along the central-northern Chile region because of the lack in wind measurements along the shoreline and of the relatively low-resolution of the available atmospheric reanalysis. Here, the seasonal variability in Ekman transport, Ekman pumping and their relative contribution to total upwelling along the central-northern Chile region (~30ºS) is evaluated from a high-resolution atmospheric model simulation. As a first step, the simulation is validated from satellite observations, which indicates a realistic representation of the spatial and temporal variability of the wind along the coast by the model. The model outputs are then used to document the fine scale structures in the wind stress and wind curl in relation with the topographic features along the coast (headlands and embayments). Both wind stress and wind curl had a clear seasonal variability with annual and semiannual components. Alongshore wind stress maximum peak occurred in spring, second increase was in fall and minimum in winter. When a threshold of $-3x10^{-5}$ s^{-1} for the across-shore gradient of along-shore wind was considered to define the region from which the winds decrease toward the coast, the wind drop-off length scale varied between 8 and 45 km. The relative contribution of the coastal divergence and Ekman pumping to the vertical transport along the coast, considering the estimated wind drop-off length, indicated meridional alternation between both mechanisms, modulated by orography and the intricate coastline. Roughly, coastal divergence predominated in areas with low orography and headlands. Ekman pumping was higher in regions with high orography and the presence of embayments along the coast. In the study region, the vertical transport induced by coastal divergence and Ekman pumping represented 60% and 40% of the total upwelling transport, respectively. The potential role of Ekman pumping on the spatial structure of sea surface temperature is also discussed.

54 Keywords: drop-off, wind curl, upwelling, Ekman pumping

1. Introduction

In the eastern boundary current systems wind-induced upwelling has mainly been described using two primary mechanisms (Sverdrup et al., 1942; Gill 1982; Pickett and Paduan, 2003; Capet et al., 2004; Jacox and Edwards, 2012). The first one is coastal divergence which is the result of offshore Ekman transport due to alongshore winds (with an equatorward component) and earth's rotation and the presence of the coast (i.e. coastal upwelling). The second one is Ekman pumping which is the result of a cyclonic wind stress curl caused mainly by the wind drop-off that extends only tens of km in width along the coast, and is a typical feature of the eastern boundary current systems (Bakun and Nelson, 1991; Pickett and Paduan, 2003; Capet et al., 2004; Jacox and Edwards, 2012). Starting in the mid 1970s, a series of studies began assessing the contribution of Ekman pumping on coastal upwelling for the California Current System (Halpern, 1976; Nelson, 1977), which later expanded to the other four upwelling systems (Bakun and Nelson, 1991). In one of these four regions, the coast of north and central Chile, this mechanism has been poorly evaluated, primarily due to the scarcity of *in situ* data, limitations in diffusiometer winds that have a "blind zone" near the coast and the relatively low spatial resolution of the atmospheric reanalysis. This has caused a limited progresses in the understanding of the upwelling dynamics and the coastal circulation of the region, among other factors.

Coastal upwelling has been widely studied in several regions of the world, in particular along the Eastern Boundary Upwelling Systems (EBUS). Currently, there is no generalized conceptual model for the upwelling structure that considers the region near the coast, the coastal boundary and the open ocean (Mellor, 1986; Marchesiello and Estrade, 2010). Traditionally a simple relationship based on wind stress along the coast has been used as an index of the coastal upwelling intensity (Bakun, 1973), this approximation does not consider other more complex physical processes, such as the wind curl (Pickett and Paduan, 2003; Capet et al., 2004; Jacox and Edwards, 2012) and the geostrophic flow toward the coast, which is in balance with the along shore pressure gradient and could potentially limit upwelling (Marchesiello et al., 2010; Marchesiello and Estrade, 2010). In the case of the wind curl, several modeling studies from different

upwelling systems suggest that wind stress decreases within a narrow coastal band of 10-80 km called wind "drop-off" (Capet et al., 2004; Bane et al., 2005; Perlin et al., 2007; Renault et al., 2012; Renault et al., 2015) that is highly sensitive to the resolution of the model. Thus, regional ocean modeling studies show that the upwelling response is sensitive to the transition in the structure of the wind near the coast (Capet et al., 2004; Jacox and Edwards, 2012), where the structure and physical forcing of the transitional coastal wind profile is not well understood (Jin et al., 2009). In the literature at least three main hypotheses have been proposed to explain the weakening of the wind close to the coast (drop-off) that generates the wind stress curl within the coastal band. The first is related to the change of surface and boundary layer friction in the land-sea interface (Capet et al., 2004). The second is related to the ocean-atmosphere coupling between the sea surface temperature (SST) and the wind (Chelton et al., 2007), particularly cold water upwelling tend to stabilize the atmospheric boundary layer, decoupling the high atmospheric circulation from the surface circulation. The last one is related to coastal orography (Edwards et al., 2001), coastline shape (Perlin et al., 2011), and the combination of both (Renault el at., 2015) constraining the vorticity budget of the low-level atmospheric circulation. Other possible mechanisms that could potentially contribute to wind drop-off near the coast are the effects of sea breeze and pressure gradients (across or along the coast) at sea level.

The central-northern Chile region is characterized by nutrient rich cold surface waters, attributed to the surface circulation of the Humboldt system and mainly coastal upwelling driven by along shore winds that are associated with the southeast Pacific anticyclone (Shaffer et al., 1999; Halpern, 2002). A strong seasonal variability of the southeast Pacific anticyclone produces favorable upwelling winds to peak during spring and summer and decrease during winter (Strub et al., 1998). Within central-northern Chile the area around 30°S is characterized by the most intense upwelling favorable winds (Shaffer et al., 1999; Rutllant and Montecino, 2002). Additionally, local high frequency forcing in the region is associated with atmospheric coastal jets with periods less than 25 days, that are related to synoptic dynamics of the mid-latitude pressure perturbations, in this case high pressures, that migrate toward the east (Muñoz and Garreaud, 2005; Rahn and

Garreaud, 2013) and play a major role in coastal upwelling (Renault et al., 2009, 2012; Aguirre et al., 2012). All these features make the region a natural laboratory to explore the forcing mechanisms and describe the physical processes that modulate coastal upwelling.

In a recent modeling study Renault et al. (2012) analyzed the main physical processes that explain changes in sea surface temperature in an upwelling event during the occurrence of an atmospheric coastal jet along the central-northern Chile region. The results showed a clear drop-off of the coastal wind that was not observed in the QuikSCAT data, due to the "blind zone" in the satellite measurements (~25 km offshore). The oceanic response to the atmospheric coastal jet produced significant cooling of the sea surface that significantly contributed to ocean vertical mixing equivalent to the magnitude of the vertical advection near the coast. Their sensitivity analyses showed that the response of the coastal ocean highly depends on the representation of the wind drop-off. This is because the total upwelling (*i.e.* the sum of coastal upwelling and Ekman pumping) depends on the scale of the wind drop-off. The authors suggest that there is a negative effect on coastal upwelling, due to a reduced Ekman transport near the coast that is not balanced by Ekman pumping. In addition, the drop-off has a strong effect on vertical mixing and consequently the cooling of the coastal ocean. In a previous modeling study Capet et al. (2004) off the coast of California suggested that a poor representation of the wind drop-off could underestimate Ekman pumping and overestimate coastal upwelling (and vice versa), with consequences for the coastal circulation processes. Meanwhile, Garreaud et al. (2011) using observations found a local atmospheric coastal jet just north of one of the most prominent geographic points of the region: Punta Lengua de Vaca (see Fig. 1). This coastal jet shows a distinct daily cycle as the result of the strong baroclinicity due to heating differential in the region. In a later study Aguirre et al. (2012) using climatological QuikSCAT winds to force a regional ocean model, found the importance of the wind stress curl over the regional circulation exerting control over the seasonal cycle of an Equatorward coastal jet. This study also evaluated the contribution of Ekman pumping to the total upwelling, which was not well resolved due to a poor resolution of the satellite winds within the first 30 km near the coast. In particular, due to

148 the narrow continental shelf off central-northern Chile, the cells of upwelling due to
149 coastal divergence are trapped near the coast (Estrade et al., 2008), consequently the use
150 of QuikSCAT winds could be overestimating the effect of upwelling driven by coastal
151 divergence and Ekman pumping.
152
153 Although previous studies have documented the importance of the wind stress curl near
154 the coast of central Chile (Renault et al, 2012; Aguirre et al, 2012), the impact of the
155 abrupt transition of the wind near the coast (*i.e*. drop-off) and its seasonal variability on
156 upwelling are still poorly understood. Here, prior to addressing this issue from an oceanic
157 perspective, our objective is to document the wind stress curl (drop-off) and its seasonal
158 variability off central-northern Chile (~30°S) using a high resolution (~4 km)
159 atmospheric model. Our focus in on the Ekman pumping and its contribution to the total
160 upwelling, and the factors that could contribute to its meridional variability (*i.e*.
161 topography, coastline and air-sea interactions).
162
163 The paper is organized as follow: a description of the atmospheric simulations and the
164 methods used to estimate different upwelling terms are described in section 2. The
165 section 3, presents results and discussions and was subdivided into four subsections. The
166 first one describes wind stress curl pattern and the spatial scale of the wind drop-off. The
167 second and third, presents an analysis of the annual variability in Ekman Pumping and
168 coastal divergence, and their relationship with coastal topography and their contribution
169 to upwelling transport. The fourth relates the study relates Ekman Pumping transport to
170 sea surface temperature near the coast. Finally, section 4 presents a summary.
171
172 **2 Methods and Model Configuration**
173 2.1 Model Output
174
175 The Weather Research and Forecasting (WRF) model version 3.3.1 (Skamarock and
176 Klemp, 2008) was configured with three nested domains (Fig. 1) with increasing
177 horizontal grid spacing over the region of interest by a factor of 3 from on domain to the
178 next. The largest synoptic domain covers most of South America and the eastern Pacific

179 in a Mercator projection with a horizontal resolution of 36 km. The northerly extension of
180 the parent domain extend to 10ºN because beyond the focus of the present study we are
181 also interested (future work) in assessing the impact of the downscaled winds from the
182 coarse domain over a regional ocean model of the Humboldt system whose domain
183 extends from 5ºN to 40ºS following the approach of Cambon et al. (2013). The second
184 domain covers the coast of north-central Chile (25°-35° S) with a horizontal resolution of
185 12 km. The innermost domain is centered over the Coquimbo bay system with a
186 horizontal grid spacing of 4 km (Fig. 1). The use of such near-kilometer resolution
187 improves the representation of complex terrain and is necessary for dynamical
188 downscaling of near-surface wind speed climate over complex terrain (Horvath, 2012).
189 WRF employs a terrain-following hydrostatic-pressure coordinate in the vertical, defined
190 as eta (η) levels, here a total of 42 η levels were used in the vertical with increasing
191 resolution toward the surface, 20 of them in the lowest 1.5 km with ~30 m in the vertical
192 for the surface level, such telescopic resolution is a common choice in precedent studies
193 to properly simulate the MBL depth over the ocean (Muñoz and Garreaud, 2005; Rahn
194 and Garreaud 2013; Toniazzo et al, 2013; Renault et al 2012; Rutllant et al, 2013).
195
196 Given the complex interactions between alongshore winds, topography, cloudiness, land
197 heating and coastal upwelling in the study region (Rahn and Garreaud 2013; Wood et al.,
198 2011; Toniazzo et al., 2013) we have tested the WRF model in different combinations of
199 parameterizations (cumulus - planetary boundary layer - soil model), surface data (SST
200 forcing, topography and land surface) and nesting technique. A set of eight sensitivity
201 simulations (for more details see response to referee 1, http://www.ocean-sci-
202 discuss.net/os-2015-94/#discussion) was carried out for the control period, i.e. from 1
203 October 2007 to 31 December 2007 corresponding to the upwelling season in north
204 central Chile. The results were evaluated against surface observations from
205 meteorological automatic stations and scatterometers (QuikSCAT, ASCAT), particular
206 attention was paid to the shoreward decrease and temporal variability of the surface wind
207 speed near the coast. The configuration with the best estimates of observed surface
208 variability and mean state was then used for the long simulation 2007-2012 (Table 1).
209

The initial and Lateral Boundary and Conditions (LBC) were derived from the National Centers for Environmental Prediction (NCEP) Final Analysis Data (FNL) (Kalnay et al. 1996; available online at http://dss.ucar.edu/datasets/ds083.2/) at 1°x1° global grids resolution every six hours. The boundary conditions are prescribed over the coarser domain with the depth of 5 grid-cells where simulated variables are relaxed towards the FNL solution. The SST forcing data are based on the daily Operational Sea Surface Temperature and Sea Ice Analysis (OSTIA) at 0.05°x0.05° global grids resolution (Stark et al. 2007). To include the diurnal cycle we have calculated the 6-h anomalies with respect to the daily mean from the six hours FNL SST and then added to the daily OSTIA SST. In this way we generate the 6-h lower boundary updates with the same update rate used for the LBCs as Renault et al. 2015.

For each year the model was re-initialized with the FNL reanalysis every three months leaving 6 overlap days as a spin-up, the outputs during this period were excluded from the analysis, this scheme was suggested by Lo et al. (2008) in order to mitigate the problems of systematic error growth in long integrations and inconsistences between the flow developing and the lateral boundary conditions. The instantaneous model diagnosis were stored at hourly intervals, the time steps were set to 108, 36 and 12 seconds for the domains of 36, 12 and 4 km resolution respectively.

The simulated winds were validated using QuikSCAT and observations from two weather stations near the coast in Loma de Hueso (LDH) and Punta Lengua de Vaca (PLV) and a third station farther inland named Parral Viejo (Fig. 1 and 2). A spatial comparison for 2007-2009 was done between satellite and WRF using the coarse resolution grid (36 km). The comparison showed a good agreement between observations and modeling results with a similar spatial structure and magnitudes of the same order, especially within the study region (27ºS-33ºS). The root mean square (RMS) of the difference for observations and model results was less than 1 m s^{-1} (Fig. 2c). The high-resolution model outputs (4 km) were also compared with available observations. Initially, for each of the weather stations daily wind cycles were compared with simulations (not shown). The results indicate a better fit in diurnal variability when the model is forced

with SST (OSTIA), which was finally chosen for the simulations performed in this study. The best fit between observations and model outputs was found when the wind intensifies during the afternoon between 17 and 19 hrs. A good model representation of the afternoon winds is key for a proper representation of coastal upwelling in the region. Finally, for each weather station, linear regressions and dispersion plots were done between the meridional component of simulated (4 km) and observed winds (Fig. 2d-f). A good agreement was observed for all the cases.

2.2 Upwelling estimates

The relative importance of coastal upwelling due to coastal divergence (Smith, 1968) was estimated using wind stress obtained by the WRF model:

$$Et = \frac{1}{\rho_w f} \tau \times \hat{k} \qquad (1)$$

where Et is Ekman transport ($m^2\ s^{-1}$), τ is the wind stress at the land-sea margin (~4 km from the coast), ρ_w is water density, f is the Coriolis parameter and k is a unit vertical vector. The vertical velocity from Ekman pumping was estimated using a definition given by Halpern (2002) and Renault et al. (2012).

$$w_{EP} = \frac{Curl(\vec{\tau})}{\rho_w f} + \frac{\beta \tau_x}{\rho_w f^2} \qquad (2)$$

where $\tau(x,y)$ is wind stress, β is the Coriolis parameter gradient and τ_x is the cross-shore wind stress. Latitude variations were not significant therefore the last term in equation (2) was neglected. In order to compare the two upwelling processes, Ekman pumping was converted into transport by integrating the vertical velocity within a certain distance from the coast, which in our case was the length scale of the wind drop-off (Ld) obtained from a reference value (defined by Renault et al., 2015) where cross-shore wind curl was < $-3 \times 10^{-5}\ s^{-1}$. The wind drop-off spatial length (Ld) varies meridionally (Fig. 3b-c).

Note that if we assume that the wind is parallel to the coast and that the wind curl is dominated by its cross-shore gradient component (and this gradient is nearly constant in the drop-off zone), then the total upwelling transport is simply $\tau/(\rho f)$ or expressed as vertical velocity is $W = \tau/(\rho f L_d)$, where τ is the wind stress at L_d. Consequently it is apportioned to Ekman transport and pumping according to the amount of drop-off (for more details see Renault et al., 2012). On the other hand, in our study region there is a marked decline toward the coast of the meridional wind component, therefore the wind drop-off has an impact on the total upwelling velocity. Thus a proper assessment of scales involved in both mechanisms is crucial to the upwelling problem.

3 Results and discussion

3.1 Mean wind stress curl and the wind drop-off spatial scale

From the wind stress simulations (model wind outputs) we obtained the mean of the wind stress curl in the three model domains with spatial resolutions of 36, 12 and 4 km (Fig. 3a-c). The mean wind stress curl patterns show clear differences when resolution is increased. In the simulations of higher resolution small scale or finer structures are well defined, especially close to the coast, that are not present in the simulation of coarse resolution, and that are not resolved or studied in previous studies (Aguirre et al., 2012; Renault el al., 2012). The simulations with higher resolution (12 and 4 km) show a cyclonic wind stress curl (negative) within the coastal band and within the Coquimbo bay system that is associated to a positive Ekman pumping (producing upwelling). While in the oceanic sector a less intense anticyclone wind curl predominates. The negative curl within the coastal band is the result of an onshore decay in wind intensity (drop-off) that is characteristic from EBUS systems (Capet et al., 2004; Renault et al., 2012).

In the central-northern Chile region the drop-off length scale (Ld) is between 8 and 45 km (Fig. 3b-c, segmented yellow line). When the resolution of the model is increased, the wind drop-off takes place closer to the coast and exhibits a larger meridional/latitudinal variability, with in particular a larger drop-off scale in the central region of the domain than in the region south of 30.25°S. The meridional differences of Ld could be associated to coastal orography and the shape of the coastline; this will be discussed later in section 3.3. The finer structures in the wind stress curl close to shore, cannot be determined with confidence from observations of the scatterometers of previous and current satellite missions, such as QuikSCAT and/or other satellite, because of the blind zone in measurements within the first 25 km from the shore. Note that the blind zone increases to 50 km when wind stress curl is estimated, as the result of the estimate of the spatial derivative.

Renault et al. (2012) based on atmospheric simulations (obtained with WRF) determined that the extent of the wind drop-off was ~70 km. This length was different from the one

obtained in this study (which varied between 8 and 45 km), possibly because of the lower resolution used in their study. To further explain the zonal wind structure and drop-off, Figure 3d shows zonal profiles of the meridional wind of the more exposed region. The results indicate a clear decay of the wind along the coast in the three simulations (36, 12 and 4 km) that is not observed in the satellite data from QuikSCAT. It should be noted the small difference with the satellite product. As mentioned above, in the study region there is a lack of wind information within the coastal band that covers the blind zone of the satellites and that can be used for validation purpose. One of the first in situ measurements in the region were done during the field campaign CupEX (Garreaud et al., 2011). During this experiment a zonal profile of wind was measured using airborne meteorological techniques. These observations allowed detecting an atmospheric coastal jet with a marked daily cycle that extended north of Punta Lengua de Vaca towards the Coquimbo bay system.

Such a coastal jet is present in our simulations that produce a wind curl in the bay system, which affects the circulation and coastal upwelling in the region. Other recent wind observations were collected under the scope of this study (FONDECYT Postdoctoral project 3130671), and are presented in Figure 3e. These wind observations were made with a marine weather station (AirMar) installed on a fishing boat. Measurements were made for 04/22/2014, 05/18/2014, 09/15/2014 and 10/28/2014. Although these measurements do not cover the period of the simulations, they are presented here to illustrate observed features of the zonal wind profiles in the southern region. Despite the large spatial and temporal variability of the observations, they suggest a tendency to a reduction of the along-shore winds toward the coast comparable to what is simulated by the model (Fig. 3d).

Focusing now on the model results, in our study region the atmospheric coastal jet extends from the coast for several tens of kilometers to the west, showing some nearshore maximums, like in Punta Lengua de Vaca (Garreaud and Muñoz, 2005; Muñoz and Garreaud, 2005, among others). In addition, near Punta Lengua de Vaca the atmospheric local and baroclinic jet (local origin), with a marked diurnal cycle has a maximum around 18:00 (local time) (Garraeud et al, 2011; Rahn et al, 2011). We compared the differences between using of WRF wind averaged only during afternoon hours and wind averaged

daily during the spring months (not shown). The simulation showed an intensification of the wind in the afternoon, emphasizing the coastal jet at Punta Lengua de Vaca (~30.5°S, south of Tongoy Bay), strong winds were also observed north of Punta Choros (29°S) and south of 31°S. However, when we used the daily averages, we can distinguish the coastal jet and high winds in Punta de Choros and south of 31°S, but with smaller magnitudes than in the afternoon. This is due to the smoothing produced by the averaging to daily mean data. On the other hand, if we look at the structure of Ekman pumping for the two cases, all showed a similar pattern near the coast, with a positive values (favorable to upwelling), but differed in their magnitude, which was greater in the afternoon. Therefore, we believe that for the purposes of this manuscript, using daily averages of wind from the WRF simulation time was valid.

3.2 Annual variability of the wind stress and Ekman pumping

The seasonal analysis of the wind stress and the Ekman pumping is based on the simulation having the highest resolution (4 km), considering the daily average from instantaneous wind values with an hourly sampling over the period between 01/01/2007 and 12/31/2012. Figure 4 presents the mean seasonal cycle of the wind stress for the study area in the coastal fringe extending 150 km from the coast. The wind stress presents a seasonal and spatial variability, with predominance of upwelling favorable winds (with equator-wards component) during all the year round, with maximum values (~0.15 N/m^2) between September and November, which is characteristic of the central-northern region of Chile (Shaffer et al., 1999, Rutllant and Montecino, 2002, Ranh and Garreaud, 2013). The seasonal variability of the wind stress determines the behavior of the coastal upwelling and primary productivity in the region. This is through two main mechanisms, the coastal divergence and the Ekman pumping, that will be evaluated in the following section. The wind also induces vertical mixing and surface cooling. This cooling effect can be even comparable to the one by vertical advection (Renault et al. 2012). In general, these mechanisms may covary in time, responding to the seasonal cycle of the wind stress; hence in a grouped statistical analysis (like SVD) it is difficult to isolate the spatio-temporal combined variability of two mechanisms without rejecting the effect of the third. On the

385 other hand, the model simulates well the coastal atmospheric jet observed in the zone of
386 Punta Lengua de Vaca (~30ºS), in particular the maximum intensity during spring (Rahn
387 and Garreaud, 2011; Rahn and Garreaud, 2013).
388
389 Close to the coast, where the satellite data have no coverage or the estimate in wind stress is
390 uncertain (Fig. 1), a wind decay towards the coast (drop-off) is observed during practically
391 all the calendar months of the year, with still a more pronounced tendency in the period
392 between September and December. The horizontal gradient of the wind stress that is most
393 intense close to the coast produces a wind curl with a clockwise rotation direction (cyclonic
394 for the SH) generating a positive Ekman pumping favorable to the upwelling.
395
396 In addition to a non-uniform spatial distribution, the drop-off length (Ld) in the area of
397 interest also exhibits a marked seasonal variability. Based on an atmospheric simulation in
398 the west coast of USA, Renault et al. (2015) also suggested that the drop-off presents
399 seasonal and spatial variability, but with an extension ranging from between 10 to 80 km.
400 These authors propose that the drop-off dynamics of the wind is due mainly to orographic
401 effects and the shape of the coastline, reaching a maximal reduction of the wind (~80%)
402 when these are combined. According to these authors, the drop-off length scale of the wind
403 in front of Chile should be approximately 30 km, less than the scale off the west coast of
404 USA. This would result from the different shape of the Chilean coastline characterized by a
405 straighter coastline and the reduced numbers of capes compared to the US West coast. In
406 addition the Andes would induce a sharper onshore decline of the wind (drop-off) than the
407 mountains of the west coast of the USA (Renault et al., 2015). In the section 3.3 the length
408 scale of the drop-off along the central-north coast of Chile will be analyzed in relation with
409 the coastal orography and the shape of the coastline.
410
411 Despite that the length scale of the wind drop-off in front of central-northern Chile (~45 km)
412 is on average less than that estimated in the California currents system (Enriquez y Friehe,
413 1996; Renault et al., 2015), the wind-stress curl from this zonal gradient of the wind
414 generates an Ekman pumping with a marked seasonality (Fig. 5) and positive vertical

velocities (upward) that reach 4 m day^{-1}, similar values to that obtained by Pickett and Paduan (2003) in front of the region of the California current system.

The simulation (4 km) has allowed to depict and document the mesoscale atmospheric circulation in the first 50 km from the coast (Fig. 3), where the spatial patterns of the Ekman pumping are much more marked, especially at latitudes where there are sharp topographic changes in the coastline (Fig. 5). Thus, structures of Ekman pumping are highlighted to the north of the main headlands of the region (Punta Lengua de Vaca and Punta Choros), and experience a seasonal cycle. In addition, the Ekman pumping presents negative values (downwelling) off shore associated to an anti-cyclonic wind curl around 28.5°S and between 30°S and 31°S that reaches the greatest extent during August, while decreasing considerably in the summer months and beginning of fall (Fig. 5). Mean Ekman pumping in spring is much larger than in the other seasons (*i.e.* summer, fall and winter) indicate that the spring positive pumping dominates the other, specially north of 29ºS, in the interior of the Coquimbo bay system and south of 31.5ºS (not shown).

With the objective of analyzing in more details the seasonal and spatial variability of the wind stress and its zonal gradient, three specific sectors of the study area were selected (28.5º, 30.5º and 32.5ºS), that are outside of the Coquimbo bay system (Fig. 6). As was mentioned before, the region is characterized by a marked wind stress seasonality more pronounced to the south of the study area (Fig. 6c). In general, the wind component along the coast shows a predominance of southerly winds favorable to the upwelling during all the year round, emphasizing a decrease in the wind stress towards the coast for the spring and summer months at 32.5ºS, and in summer at 28.5ºS and 30.5ºS. When estimating the zonal gradient of the wind stress taking as a reference the wind at the coast, the most intense positive gradients (due to the wind drop-off towards the coast) are obtained in a coastal band with a width smaller than 50 km, indicating that the Ekman pumping is the most effective inside the coastal band, as is evidenced in the Figures 4 and 5. On the other hand, the negative zonal gradient extent (Ekman pumping and downwelling) is greater in the sections located farther the north, at 28.5°S and 30.5°S, than in the section located at 32.5°S (Figs. 6 d, e and f), indicating that in the southern part of the study region, the

positive Ekman pumping region extends farther than in the zones where the wind stress is more intense seasonally close to the coast (Fig. 4).

3.3 Contributions of Ekman transport and Ekman pumping to the upwelling rate

The central-northern Chile continental shelf is very narrow and very steep so the scale of coastal divergence is <10 km (considering the theoretical framework of Estrade et al., 2008), while the length scale Ld of Ekman pumping (previously defined, based on Renault et al., 2015) is ~45 km. To compare the seasonal contribution of coastal divergence and Ekman pumping to the total transport of coastal upwelling in the study region, the annual cycle of coastal divergence was obtained first by taking the wind of WRF closest to the coast (< 8 km) and meridionally integrated every 0.25° (Fig. 7e), while the annual cycle of Ekman pumping transport (from wind of WRF) was obtained by integrating the vertical velocity from the shoreline to the distance corresponding to the drop-off (Ld) value, also within 0.25° latitude bands (Fig. 7f).

The results indicate a marked annual cycle with maximum vertical transport in the spring, both induced by coastal divergence and Ekman pumping, with secondary maximum in some areas during autumn accounting for a weaker semiannual component. As expected, there is a large temporal coherency along the coast between both processes (the meridional average correlation between Ekman pumping and coastal divergence reaches 0.8), except locally at some latitudes (e.g. at 31.25°S) where there is a weak seasonal cycle in Ekman pumping (Fig. 7f) due to either a weak drop-off or a compensation effect by the zonal wind stress component. The high correlations indicate a seasonal consistency between both mechanisms, which has been previously reported in other upwelling systems (e.g. Pickett and Paduan, 2003; Renault et al., 2015). Although both mechanisms are highly correlated at seasonal timescales, they exhibit significant differences in relative magnitude as a function of latitude, *i.e*. when one is intense the other is weak. For instance, coastal divergence strongly dominates over Ekman pumping between 30.25ºS - 31.25ºS (Fig. 7d), which is the most recognized upwelling center in the region (located south of PLV), as well as in the region between 28.5°S - 29.25ºS (north of Punta Choros). In those regions Ekman pumping

tends to be weaker, whereas it is predominant for the area between 29.25 - 30.25ºS, inside the Coquimbo bay system and the area between 28.0ºS - 28.75ºS, north of LDH. South of 31.25°S, both mechanisms vary meridionally more uniformly. The estimate of the meridional correlation between both mechanisms as a function of calendar month indicates that they are better related in spring and summer (~-0.72) than in winter (~0.45). Possible processes that could explain the inverse (negative) spatial relationship between the two mechanisms and its seasonal modulation are discussed below. Before continuing, we should mention that processes such as upwelling shadow can be important in the Coquimbo bay system, and would affect the temperature distribution inside the bay, especially in the southern part of the bay close to the coast, where higher temperatures are observed (and higher thermal front) compared to the lower temperature area that extends north from Punta Lengua de Vaca (Figure 10). In fact a study in the southern part of the Coquimbo bay system (Moraga et al., 2011) shows cyclonic circulation when there are upwelling favorable winds, the circulation is attributed to the separation of oceanic flow in Punta Lengua de Vaca, which is in agreement with the process of upwelling shadow and mainly affects the area indicated above. However, we think that this is not inconsistent with the effect of the wind curl in the area, which would favor upwelling north of Punta Lengua de Vaca. The oceanic response in the area clearly needs more attention and research in future.

Considering the influence of topography and the geometry of the coastline to describe the spatial variability of the wind stress, (e.g. Winant et al., 1988; Burk and Thompson, 1996; Haack, et al., 2001; Koracin et al., 2004; Renault et al., 2015, among others), we now document the relationship between the relative importance of Ekman transport and pumping, and the coastal topography and shape of the coastline in the region. An along-coast orography index (H_{index}) is estimated from the average of the orographic height between the coastline and 100 km inland (as in Renault et al. 2015). In addition, the coastline meandering index (M_{index}) is estimated by converting the position of the coastline into distances and afterward using a high variability-pass filter (with 10 km half- width) the small fluctuations in the index are smoothed, consequently the index only considers the abrupt change in coastline configuration at relatively large scale (Renault et al., 2015). Figure 7a shows the H_{index} (black line) and M_{index} (red line). In the latter index negative

values are associated with headlands, while positive values are associated with bays. The drop-off scale and alongshore wind at the coast and at Ld are also included (Fig. 7b-c). Note that Ld is inversely proportional to coastal wind (R^2 de ~0.81), while the wind evaluated at Ld is spatially more homogenous. This differs from the results obtained by Renault et al. (2015) along the western coast of USA. From the inspection of H_{index}, M_{index} and Ld three scenarios are defined that could explain the observed upwelling pattern (Fig. 7d-f):

1. Prevalence of positive Ekman pumping: in sectors such as the Coquimbo bay system and the region north of 28.5ºS (LDH), where the wind curl intensifies due to the sharp decline of onshore wind, with a large drop-off scale (Ld). In addition, the combination of a high orography (large H_{index}) and the presence of bays favor a decrease in the meridional onshore wind.

2. Prevalence of coastal divergence: in sectors characterized by a low topography (small H_{index}) and a negative M_{index} due to the presence of headlands such as Punta Lengua de Vaca and Punta Choros, with a smaller drop-off scale (Ld) and stronger winds alongshore (Fig. 7b-c).

3. South of 31.25°S the pattern is more complex than previous scenarios. Both mechanisms are present but with a slight dominance of coastal divergence compared with Ekman pumping. South of this latitude, Ld increases, coastal wind decreases and wind curl increases (Fig. 7b-c). M_{index} shows the presence of small inlets and headlands and the orography index is moderate high without largest changes as in the northern coastal region.

Renault et al. (2015) proposed that the coastal topography induces a decrease in the intensity of the wind towards the coast through the vortex stretching term. Similarly, Archer and Jacobson (2005) from atmospheric numerical simulations showed that the topography in the Santa Cruz-California region, is required for the formation of turbulence and vorticity. On the other hand, the shape of the coastline with capes and headlands increases the orographic effect through the vortex stretching term, tilting-twisting and

539 turbulent flux divergence (Archer and Jacobson, 2005; Renault et al., 2015). The sea-land
540 drag coefficient difference mainly acts as a barrier that turns the wind alongshore.
541
542 Another minor factor is the sharp coastal sea surface temperature front associated with
543 upwelling. Renault et al (2015) show that in their sensitivity experiment adding a sharp
544 SST front over a coastal band strip leads to weaker surface wind associated with more
545 stable and shallow marine boundary layer. This response of wind may be due to so-called
546 "downward mixing" mechanism (Wallace et al., 1989; Hayes et al., 1989), which was used
547 by many authors to explain the observed tendency of surface winds to decelerate over
548 colder flank of the SST front and accelerate over warmer flank of the SST front (*cf*. Small
549 et al., 2008 and references therein): warm (cold) SST would destabilize (stabilize) the PBL
550 and cause enhanced (reduced) vertical turbulent mixing, increasing (decreasing) downward
551 fluxes of horizontal momentum from the faster flow above to the slower near-surface flow.
552 Nevertheless, a large SST anomaly (by −3 ºC in the experiment of Renault et al., 2015) is
553 needed to induce a significant weakening of wind and significant additional wind drop-off.
554 Therefore, the SST effect can be considered as secondary compared to the orography effect
555 over the California coast.
556
557 The combination of coastal topography and the presence of headlands, points and capes on
558 the United State (US) west coast, induces a stronger and larger wind drop-off, which in turn
559 is associated with a positive Ekman pumping (Koracin et al., 2004; Renault et al., 2015).
560 This characteristic differs from what is observed along central-northern Chile, where the
561 larger drop-off (Ld) length, associated with a strong wind curl (Fig. 7b-c), takes place in the
562 presence of abrupt orography and within the Coquimbo bay system (30.25ºS - 29.25ºS).
563 There the cross-shore wind component is more intense and favors the wind curl, whereas
564 with lower terrain and the presence of headlands the Ld is very small (*cf*. Fig. 10, Renault et
565 al., 2015). The origin of these differences is not well known; they may be due to several
566 factors or processes. For instance, the topographic terrain along the coast of northern Chile
567 is much higher (for the coastal range and Andes mountains) than the terrain along the west
568 coast of the US. Furthermore, a feature of particular interest north of Punta Lengua de Vaca
569 is the presence of the local atmospheric jet, which has a strong diurnal cycle and a clear

570 seasonal variability, as a result of coastal topography that favors baroclinicity north of PLV
571 (Garreaud et al., 2011; Rahn et al., 2011). This feature would deserve further consideration
572 based on the experiments done with the regional atmospheric model, however this is
573 beyond the scope of the present study. Here the focus is on understanding possible effect of
574 the wind drop-off and its spatial and seasonal variability on the upwelling dynamics.
575
576 To determine the contribution of the two proposed mechanisms to the total upwelling in the
577 region, vertical transport due to coastal divergence and Ekman pumping were meridionally
578 integrated (from Fig. 7e and 7f, respectively). The contributions of both mechanisms to
579 upwelling (Fig. 8) have a clear annual cycle with a marked semiannual component.
580 Maximum values occur during October, with 0.23 and 0.14 Sv for coastal divergence and
581 Ekman pumping, respectively, while the sum of both is 0.37 Sv. Coastal divergence and
582 Ekman pumping represent 60% and 40% of the total upwelling, respectively. This indicates
583 that coastal divergence is the stronger upwelling mechanism. However, it should be noted
584 that these values are the sum throughout the region, and these percentages would change if
585 specific sectors were considered especially where Ekman pumping has a larger significance
586 (Fig. 7).
587
588 Comparing our estimates with those obtained by Aguirre et al. (2012) from QuikSCAT
589 wind information using a larger region (~27.5°S - 40°S), it is observed that coastal
590 divergence from our study is lower, mainly because they estimated averages using only 2
591 values every day, which may influence the daily mean and therefore their estimates. Also
592 their analysis did not include the wind drop-off area. The winds used in their study are
593 stronger and so are their estimates for coastal divergence (*cf.* Fig. 7, Aguirre et al., 2012).
594 However, for Ekman pumping our results are only slightly smaller than theirs. This
595 difference is mainly due to differences in the method employed to estimate the vertical
596 upwelling transport. In particular they use a length scale (Ld) of 150 km from the coast for
597 their calculation, while in this study a value of 45 km was considered. However, the largest
598 differences in the estimates of the contributions of both mechanisms to total upwelling are
599 in the seasonal variability and the relative contribution to Ekman pumping. The seasonal
600 variability is composed of an annual cycle with a significant semiannual component,

whereas that obtained by Aguirre et al., (2012) is rather dominated by the annual cycle. This is because their estimates are based on the average over a larger region that includes the central-southern Chile region, where the wind has a significant annual variability. Moreover, the present results show a higher relative contribution of Ekman pumping to total upwelling in our region. This is partly due to a different technique for estimating this mechanism, the use of different wind products and the differences in the length of both study areas.

3.4 Annual variability of Ekman Pumping and its relationship with Sea Surface Temperature near the coast

A link between SST and wind is found throughout the world's ocean wherever there are strong SST fronts (see review by Xie, 2004; Chelton et al., 2007; Small et al., 2008). This link raises the questions of to what extent the wind-drop off could be associated to marked upwelling fronts in EBUS. In the context of our study, it consists in evaluating the relationship between Ekman pumping and SST, considering that the difficulty to tackle this issue is related to the fact that there is a large temporal coherence between Ekman pumping and coastal divergence, preventing a clear identification of Ekman pumping-induced SST anomalies where both processes are in phase. As an attempt to identify regions where Ekman pumping has an imprint on SST, we use the Multi - Scale Ultra - High Resolution SST data set (MUR, http://mur.jpl.nasa.gov) with a spatial resolution of 1 km, which was shown to better capture SST fronts than other products off Peru (Vazquez et al., 2013). Figure 9 shows the annual cycle of the MUR SST. The satellite data were compared to *in situ* observations that were obtained from 13 thermistors positioned close to surface along the coastline between 28ºS–32ºS (these observations were obtained by Centro de Estudios Avanzados en Zonas Aridas, Coquimbo, Chile) covering the period 09/2009–09/2012. The correlations obtained between observations and satellite data were high (0.74-0.94; most values were greater than 0.8) and the RMS between their differences was low varying between 0.54 and 1.3°C. This provided confidence to use MUR temperatures close to the coast in the spatio-temporal analysis done in the study region. The MUR data showed that south of 28.5°S there is a persistent surface cooling through all the year that increases in

632 extent (offshore) from ~10 km in the northern region to ~100 km in the southern region.
633 Within this region there are prominent upwelling centers, Punta Lengua de Vaca (~30.5ºS),
634 Punta Choros (~29ºS) and the region between 30.5°S – 33°S. During most of the year a
635 cold surface tongue extends from the south towards the great system of embayments of
636 Coquimbo (with limits between ~29.25°S and 30.25°S), north of Punta Lengua de Vaca. A
637 less intense cold surface tongue but with a similar structure is observed north of Punta
638 Loma de Hueso (~28.8ºS).
639
640 An illustration of the effect of Ekman pumping on SST is presented in Figure 10 which
641 shows the October mean spatial distribution for wind stress, Ekman pumping, SST and SST
642 gradient. This month was selected because the maximum values of wind stress and
643 increased surface cooling are recorded during this period. During this month, the wind
644 stress (Fig. 10a) was intense with maximum values of ~0.15 Nm^{-2}, showing a clear zonal
645 gradient (drop-off) over the entire coastal band of the study area. Note that the maximum
646 wind stress is north of the two most prominent headlands of the region (PLV and LDH),
647 right where the wind abruptly changes direction, creating an intense cyclonic wind curl
648 north of both headlands. As the result from the distribution pattern of the wind stress, wind
649 curl was negative in much of the area of interest resulting in a positive Ekman pumping
650 with vertical velocities of up to 4 m day^{-1} near the coast (Fig. 10b). Also, there are two
651 areas with a slightly negative pumping (light blue regions), following the pattern of the
652 wind stress where the wind decreases away from the coast (see the wind vectors),
653 producing a positive curl and a negative Ekman pumping. Moreover, as mentioned above
654 (see Fig. 7), much of the southern spatial structure in Ekman pumping appears to be
655 associated to the coastal terrain and abrupt changes of the coastline. A good example of this
656 is the tongue-shaped structure that extends from the upwelled waters north of Punta Lengua
657 de Vaca entering the Coquimbo bay system, where the upwelling induced by the Ekman
658 transport seems not affected (Fig. 7). As the result of a positive Ekman pumping, cold
659 water rises to surface causing a decrease in sea surface temperatures in large part of the
660 coastal region (Fig. 10c). However, this cooling is not necessarily caused by Ekman
661 pumping throughout the region, there are other processes that would contribute to the
662 surface cooling that will be discussed later. Despite this, the cooling inside the Coquimbo

663 bay system seems to be caused largely by Ekman pumping. Moreover, outside the
664 Coquimbo bay system high values (>2° C km^{-1}) of the horizontal SST gradient magnitude
665 are distributed in a band near the coast, but not attached to it (Fig. 10d) as expected for
666 upwelling fronts. Within the Coquimbo bay system, there is a homogeneous temperature
667 zone, delimited by a less intense gradient in the west and a greater gradient in the smaller
668 bays of the system, which coincides with the structure of an Ekman pumping tongue
669 projected to the north of Punta Lengua de Vaca.
670
671 In order to further document the coupled spatio-temporal patterns of Ekman pumping and
672 the SST field, a Singular Value Decomposition analysis (SVD, Venegas et al., 1997) was
673 performed. The SVD method allows determining statistical modes (time/space) that
674 maximize the covariance between two data sets. Filtered time series (low pass filter with
675 mean half-power of 280 days) and normalized of Ekman pumping and SST-MUR for the
676 2007-2012 period were analyzed using this method (Fig. 11). In this case the SVD analysis
677 was successful in capturing a dominant seasonal mode. The first dominant mode accounts
678 for 99% of the covariance, with a 43% and 87% of the variance explained by Ekman
679 pumping and SST respectively. Ekman pumping spatial pattern presents maximum values
680 very close to the coast, primarily north of Punta Lengua de Vaca, inside the Coquimbo bay
681 system (29.3ºS–30.2ºS) and north of Punta Choros (28ºS - 29ºS). Also, the pattern is
682 intense near the coast between 30.2ºS (south of PLV) and 32.5°S. The spatial pattern for
683 SST presented areas with high variability associated with areas of maximum Ekman
684 pumping, highlighting the overall variability in the bay system of Coquimbo and the area
685 north of Loma de Hueso (~ 28.8°S). Moreover, the correlation between the time series of
686 expansion coefficient was -0.96 (with R^2 = 0.92 and significant at 95 %), indicating a
687 strong inverse relationship, consistent with that expected for a positive pumping with
688 upward vertical velocities that causes a surface cooling in the region. This results in a
689 greater contribution to the north of headlands in the region (Punta Lengua de Vaca and
690 Loma de Hueso), even within the Coquimbo bay system, which is consistent with the
691 results observed in Figure 7. However, despite the high correlation obtained between both
692 mechanisms within the seasonal scale we cannot infer a relationship with SST only from
693 Ekman pumping, especially where Ekman transport dominates. Also, other processes such

694 as the direct effect of wind must play a significant role, eg. vertical mixing (Renault et al.,
695 2012), or processes related to mesoscale activity (filaments, meanders, eddies, etc.), which
696 are more intense south of Punta Lengua de Vaca (Hormazabal et al., 2004), and/or in
697 general processes related to ocean-atmosphere interaction (Chelton et al., 2007; Renault et
698 al., 2015).
699
700 Finally, our analysis calls for more thorough study on the temperature response to wind
701 forcing, which should involve oceanic modeling at a resolution high enough to resolve finer
702 scale processes. The oceanic model could be forced by the high-resolution atmospheric
703 simulations presented in this study, improving in terms of resolution from previous
704 modeling efforts in the region (Renault et al., 2012). The use of a high-resolution coupled
705 ocean-atmosphere model would improve our understanding of the air-sea interactions along
706 our study region. A plan for the development of such model is under way and will be the
707 focus of our next study
708
709 **4.- Summary**
710
711 The spatial and temporal variability (annual cycle) of the coastal divergence and Ekman
712 pumping, as well as their relative contribution to the total upwelling in the central-northern
713 Chile was studied using winds obtained from a nested configuration of the WRF model
714 allowing to reach 4-km resolution. The simulations showed a cyclonic wind curl (negative)
715 on the coastal-band nearshore and inside the Coquimbo bay system. This negative wind
716 curl is mainly due to the onshore decay of the wind (wind drop-off), which presented length
717 scales (Ld) between 8 and 45 km with a significant latitudinal variability. The wind drop-
718 off scale is in particular larger within 29.25°S-30.25°S and to the north of 28.5°S. When we
719 compared the drop-off scale with other upwelling regions, for example the coast of
720 California (Enriquez and Friehe., 1996; Renault et al, 2015), we find that it is smaller in our
721 study region. For instance Ld ranges from 10 and 80 km between 35°N and 45°N (Renault
722 et al., 2015). Despite such difference, the wind stress curl that resulted from this zonal wind
723 shear generated Ekman pumping with a marked seasonality and vertical velocities at the

724 surface that reached 4 m/day, values comparable to those observed in the California current
725 system.
726
727 When comparing the seasonal contribution of coastal divergence and Ekman pumping to
728 the coastal upwelling transport in northern-central Chile, we find that there is a high
729 seasonal coherence between the two mechanisms (> 0.8) with a maximum during spring.
730 However, despite this high seasonal correlation there is a spatial alternation between them,
731 that is, where one is intense the other is weak. This pattern seems to be the result of a close
732 relationship between the topography of the coast, the shape of the coastline and the spatial
733 scale of the wind drop-off. From this information we defined three scenarios that could
734 explain the pattern of upwelling in the area.
735
736 Prevalence of positive Ekman pumping associated to large Ld, observed in regions such as
737 the Coquimbo bay system and north of 28.5ºS. The combination of high terrain and the
738 presence of bays could explain the large Ld values.
739
740• Prevalence of coastal divergence with smaller values of Ld and more intense winds near the
741 coast. This is observed in sectors characterized by a low topography and the presence of
742 headlands as Punta Lengua de Vaca and Punta Choros.
743
744• Combination of both mechanisms where neither divergence nor coastal Ekman pumping
745 dominated over the other. This take place to the south of 31.5°S.
746
747 The 3-dimensional aspect of the coastal circulation in the region of interest (Aguirre et al.,
748 2012) prevents a clear identification of the role of each process on SST variability, although
749 our SVD analysis reveals areas where the similarity of the patterns of Ekman pumping and
750 SST suggests a privileged forcing mechanism like within the Coquimbo bay system and the
751 area north of Loma de Hueso (~ 28.8 °S). Further studies based on the experimentation
752 with a regional oceanic model should be carried out to better identify upwelling regimes by,
753 for instance, using the model winds documented here at different seasons to mimic changes
754 in the drop-off. Considering the rich marine ecosystem hosted by the region (Thiel et al.,

2007) our interest goes to relate aspects of the meso to submeso scale circulation (eddies and filaments) to the processes documented in this study. This is planned for future work.

Finally, the model allowed for an estimate of the near-shore (coastal fringe of ~50km) low-level circulation and evidences fine scale structure of the wind stress curl that cannot be estimated from satellite observations. Considering the overall realism of the model simulation, our study could be used to guide field experiments and gather in situ measurements in order to gain further knowledge in the processes that constrain such features

Acknowledgements

This work was financed by Postdoctoral FONDECYT/Chile Nº 3130671 and support from Centro de Estudios Avanzados en Zonas Aridas (CEAZA), Coquimbo, Chile. M. Ramos, L. Bravo and B. Dewitte acknowledge support from FONDECYT (project 1140845) and Chilean Millennium Initiative (NC120030). B. Dewitte and M. Ramos acknowledge support from FONDECYT (project 1151185). CNES (Centre National d'Etudes Spatiales, France) is thanked for financial supports through the OSTST project EBUS-South. Katerina Goubanova was supported by IRD. The contribution from two reviewers and the editor is deeply appreciated; their comments and suggestions improved and strengthen this study

5.- References

Aguirre, C., Pizarro, O., Strub, P. T., Garreaud, R. and Barth, J.A.: Seasonal dynamics of the near-surface alongshore flow off central Chile, J. Geophys. Res., 117, C01006, doi:10.1029/2011JC007379, 2012.

Archer, C. L. and Jacobson, M. Z.: The Santa Cruz Eddy. Part II: Mechanisms of Formation, Mon. Weather Rev., 133(8), 2387–2405, doi:10.1175/MWR2979.1, 2005.

Bakun, A.: Coastal upwelling indices, west coast of North America, 1946-71. U.S. Dep. Commer., NOAA Tech. Rep., NMFS SSRF-671, 103 p., 1973.

Bakun, A. and Nelson, C.: The seasonal cycle of wind stress curl in subtropical Eastern boundary current regions. J. Phys. Oceanogr., 21: 1815-1834, 1991.

Bane, J. M., Levine, M. D., Samelson, R. M., Haines, S. M., Meaux, M. F., Perlin, N., Kosro, P. M. and Boyd, T.: Atmospheric forcing of the Oregon coastal ocean during the 2001 upwelling Season, J. Geophys. Res., 110.C10S02, 2005.

Beljaars, A.C.M.: The parameterization of surface fluxes in large-scale models under free convection. Quart. J. Roy. Meteor. Soc., 121, 255–270, 1994.

Bretherton, C. S. and Park, S.: A new moist turbulence parameterization in the Community Atmosphere Model. J. Climate, 22, 3422–3448, 2009.

Burk, S. D. and Thompson, W. T. : The summertime low-level jet and marine boundary layer structure along the California coast. Mon. Weather Rev., 124, 668–686, 1996.

Cambon, G., Goubanova, K., Marchesiello, P., Dewitte, B., Illig, S. and Echevin, V.: Assessing the impact of downscaled winds on a regional ocean model simulation of the Humboldt system, Ocean Model., 65, 11–24, doi:10.1016/j.ocemod.2013.01.007, 2013.

Capet, X. J., Marchesiello, P. and McWilliams, J. C.: Upwelling response to coastal wind profiles, Geophys. Res. Lett., 31, L13311, 2004.

Chelton, D. B., Schlax, M. G. and Samelson, R. M.: Summertime coupling between sea surface temperature and wind stress in the California Current System, J. Phys. Oceanogr., 37, 495-517, 2007.

Dyer, A. J. and Hicks, B. B.: Flux–gradient relationships in the constant flux layer. Quart. J. Roy. Meteor. Soc., 96, 715–721, 1970

Edwards K.A., Rogerson A.M., Winant C.D. and Rogers D.P.: Adjustment of the marine atmospheric boundary layer to a coastal cape, J Atmos Sci 58(12), 1511–1528, 2001.

Enriquez, A.G. and Friehe, C.A.: Effects of Wind Stress and Wind Stress Curl Variability

on Coastal Upwelling J. Phys. Oceanogr., 25, 1651-1671, 1996.

Estrade, P., Marchesiello, P., Colin de Verdiere, A. and Roy, C.: Cross-shelf structure of coastal upwelling: A two-dimensional expansion of Ekman's theory and a mechanism for inner shelf upwelling shut down, J. Mar. Res., 66, 589–616, doi:10.1357/002224008787536790, 2008.

Garreaud, R. and Muñoz, R.: The low-level jet off the subtropical west coast of South America: Structure and variability, Mon. Weather Rev., 133, 2246–2261, doi:10.1175/MWR2972.1, 2005.

Garreaud R, Rutllant, J., Muñoz, R., Rahn, D., Ramos, M. and Figueroa, D.: VOCALS-CUpEx: The Chilean Upwelling Experiment, Atmos. Chem. Phys., 11, 2015–2029, doi:10.5194/acp-11-2015-2011, 2011.

Gill, A.E.: Atmosphere–ocean dynamics, International Geophysics Series 30, 403pp, 1982.

Haack, T., Burk, S. D., Dorman, C. and Rogers, D.: Supercritical Flow Interaction within the Cape Blanco–Cape Mendocino Orographic Complex, Mon. Weather Rev., 129, 688–708, 2001.

Halpern, D.: Measurements of near-surface wind stress over an upwelling region near the Oregon coast, J. Phys. Oceanogr., 6, 108–112, 1976.

Halpern, D.: Offshore Ekman transport and Ekman pumping off Peru during the 1997–1998 El Niño, Geophys. Res. Lett., 29(5), 1075, doi:10.1029/2001GL014097, 2002.

Hayes, S. P., McPhaden, M. J. and Wallace, J. M.: The influence of sea surface temperature on surface wind in the eastern equatorial Pacific: weekly to monthly variability. J. Climate 2, 1500–1506. 1989.

Hong, S. Y. and Lim, J.O.: The WRF single–moment 6–class microphysics scheme (WSM6). J. Korean Meteor. Soc., 42, 129–151, 2006.

Hormazabal, S., Shaffer, G. and Leth, O.: Coastal transition zone off Chile, J. Geophys. Res., 109, C01021, doi:10.1029/2003JC001956, 2004.

Horvath, K., Koracin, D., Vellore, R., Jiang, J. and Belu, R.: Sub-kilometer dynamical downscaling of near-surface winds in complex terrain using WRF and MM5 mesoscale models, J. Geophys. Res., 117, D11111, doi:10.1029/2012JD017432, 2012.

Iacono, M. J., Delamere, J. S., Mlawer, E. J., Shephard, M. W., Clough, S. A. and Collins, W. D.: Radiative forcing by long–lived greenhouse gases: Calculations with the AER radiative transfer models. J. Geophys. Res., 113, D13103, 2008

Jacox, M. G. and Edwards, C. A.: Upwelling source depth in the presence of nearshore wind stress curl, J. Geophys. Res., 117, C05008, doi:10.1029/2011JC007856, 2012.

Janjic, Z. I.: Comments on ‘‘Development and evaluation of a convection scheme for use in climate models.’’ J. Atmos. Sci., 57, 3686–3686, 2000.

Jin, X., Dong, C., Kurian, J., McWilliams, J. C., Chelton, D. B. and Li. Z.: SST-Wind Interaction in Coastal Upwelling: Oceanic Simulation with Empirical Coupling, J. Phys. Oceanogr. 39, 2957-2970, 2009.

Kalnay, E., and Coauthors: The NCEP/NCAR 40-Year Re- analysis Project. Bull. Amer. Meteor. Soc., 77, 437–471, 1996.

Koračin, D., Dorman, C. E. and Dever, E. P.: Coastal Perturbations of Marine-Layer Winds, Wind Stress, and Wind Stress Curl along California and Baja California in June 1999, J. Phys. Oceanogr., 34(5), 1152–1173, doi:10.1175/1520-0485(2004)034<1152:CPOMWW>2.0.CO;2, 2004.

Lo, J. C.-F., Yang, Z.-L. and Pielke, R. A. Sr.: Assessment of three dynamical climate downscaling methods using the Weather Research and Forecasting (WRF) model. J. Geophys. Res., 113, D09112, doi:10.1029/2007jd009216, 2008.

Marchesiello, P. and Estrade, P.: Upwelling limitation by geostrophic onshore flow, J. Mar. Res., 68, 37–62, doi:10.1357/002224010793079004, 2010.

Marchesiello P., Lefevre, L., Vega, A., Couvelard, X. and Menkes, C.: Coastal upwelling, circulation and heat balance around New Caledonia’s barrier reef. Mar. Poll. Bull., 61, 432– 448, 2010.

Mellor, G. L.: Numerical simulation and analysis of the mean coastal circulation off California, Cont. Shelf Res., 6, 689 –713, 1986.

Moraga-Opazo, J., Valle-Levinson, A., Ramos, M. and Pizarro-Koch, M.: Upwelling-Triggered near-geostrophic recirculation in an equatorward facing embayment, Cont. Shelf Res., 31: 1991–1999, doi: 10.1016/j.csr.2011.10.002, 2011.

Muñoz, R. and Garreaud, R.: Dynamics of the low-level jet off the subtropical west coast of South America, Mon. Weather Rev., 133, 3661–3677, doi:10.1175/MWR3074.1, 2005.

Nelson, C.S.: Wind stress and wind-stress curl over the California Current, NOAA Tech. Rep., NMFS SSRF-714, U.S. Dept. of Commerce, 87 pp, 1977.

Paulson, C. A.: The mathematical representation of wind speed and temperature profiles in the unstable atmospheric surface layer. J. Appl. Meteor., 9, 857–861, 1970.

914 Perlin, N., Skyllingstad, E., Samelson, R. and Barbour, P.: Numerical simulation of air-
915 sea coupling during coastal upwelling, J. Phys. Oceanogr., 37(8), 2081–2093,
916 doi:10.1175/JPO3104.1, 2007.
917
918 Perlin N., Skyllingstad E.D. and Samelson, R.M.: Coastal atmospheric circulation around
919 an idealized cape during wind-driven upwelling studied from a coupled ocean-
920 atmosphere model. Mon Weather Rev 139(3), 809–829, 2011.
921
922 Pickett, M. and Paduan, J.D.: Ekman transport and pumping in the California Current
923 based on the U.S. Navy's high-resolution atmospheric model (COAMPS), J. Geophys.
924 Res., 108, C10 3327, doi: 10.1029/2003JC001902, 2003.
925
926 Rahn D.A., Garreaud R. and Rutllant J.: The low-level atmospheric circulation near
927 Tongoy Bay / point Lengua de Vaca (Chilean coast 30◦S), Mon. Wea. Rev., 139: 3628–
928 3647, doi: 10.1175/MWR-D-11-00059.1, 2011.
929
930 Rahn, D. and Garreaud, R.: A synoptic climatology of the near-surface wind along the
931 west coast of South America, Int. J. Climatol., 34 doi: 10.1002/joc.3724, 2013.
932
933 Renault, L., Dewitte, B., Falvey, M., Garreaud, R., Echevin, V. and Bonjean, F.: Impact
934 of atmospheric coastal jet off central Chile on sea surface temperature from satellite
935 observations (2000–2007), J. Geophys. Res., 114, C08006, doi:10.1029/2008JC005083,
936 2009.
937
938 Renault, L., Dewitte, B., Marchesiello, P., Illig, S., Echevin, V., Cambon, G., Ramos, M.,
939 Astudillo, O., Minnis, P., and Ayers, J. K.: Upwelling response to atmospheric coastal
940 jets off central Chile: A modeling study of the October 2000 event, J. Geophys. Res.,
941 117, C02030, doi:10.1029/2011JC007446, 2012.
942
943 Renault, L., Hall, H. and McWilliams. J.C.: Orographic shaping of US West Coast wind
944 profiles during the upwelling season. Clim. Dyn., doi: 10.1007/s00382-015-2583-4, 2015
945
946 Rutllant, J. and Montecino,V.: Multiscale upwelling forcing cycles and biological
947 response off north-central Chile. Revista Chilena de Historia Natural, 75, 217-231, 2002.
948
949 Rutllant, J. A., Muñoz, R. C. and Garreaud, R. D.: Meteorological observations on the
950 northern Chilean coast during VOCALS-REx. Atmos. Chem. Phys., 13, 3409–3422,
951 doi:10.5194/acp-13-3409-2013, 2013.
952
953 Shaffer, G., Hormazabal, S., Pizarro, O., Djurfeldt, L. and Salinas, S.: Seasonal and
954 interannual variability of currents and temperature over the slope off central Chile, J.
955 Geophys. Res., 104, 29,951–29,961, doi:10.1029/1999JC900253, 1999.
956
957 Skamarock, W. C. and Klemp, J. B.: A time-split nonhydrostatic atmospheric model for
958 weather research and forecasting applications, J. Comput. Phys., 227, 3465–3485,
959 doi:10.1016/j.jcp.2007.01.037, 2008.

960 Small, R. J., deSzoeke, S.P., Xie, S.P., O'Neill, L., Seo, H., Song, Q., Cornillon, P.,
961 Spall, M. and Minobe, S.: Air-sea interaction over ocean fronts and eddies. Dyn. Atmos.
962 Oceans, 45, 274–319, 2008.
963
964 Smith, R.L.: Upwelling, Oceanogr. Mar. Bio. Ann. Rev., 6, 11-46, 1968.
965
966 Stark, J. D., Donlon, C. J., Martin, M. J. and McCulloch, M. E.: OSTIA: An operational,
967 high resolution, real time, global sea surface temperature analysis system. OCEANS 2007
968 Europe, IEEE, 1–4, 2007.
969
970 Strub, P. T., Montecino, V., Rutllant, J. and Salinas, S.: Coastal ocean circulation off
971 western south America, in The Sea, vol. 11, The Global Coastal Ocean: Regional Studies
972 and Syntheses, edited by A. R. Robinson and K. H. Brink, pp. 273– 314, John Wiley,
973 New York, 1998.
974
975 Sverdrup, H. U.: Wind-driven currents in a baroclinic ocean, with application to the
976 equatorial currents of the eastern Pacific. Proc. Natl. Acad. Sci. USA, 33, 318–326, 1947.
977
978 Tewari, M., Chen, F., Wang, W., Dudhia, J., LeMone, M. A., Mitchell, K., Gayno, M.
979 Ek, G., Wegiel, J. and Cuenca, R. H.: Implementation and verification of the unified
980 NOAH land surface model in the WRF model. 20th conference on weather analysis and
981 forecasting/16th conference on numerical weather prediction, pp. 11–15, 2004
982
983 Thiel, M., Macaya, E. ., Acuña, E., Arntz, W. E., Bastias, H., Brokordt, K., Camus, P. A.,
984 Castilla, J. C., Castro, L. R., Cortés, M., Dumont, C. P., Escribano, R., Fenández, M.,
985 Gajardo, J. A., Gaymer, C. F., Gómez, I., González, A. E., González, H., Haye, P. A.,
986 Illanes, J. C., Iriarte, J. L., Lancellotti, D. A., Luna-Jorquera, G., Luxoro, C., Manriquez,
987 P. H., Marín, V., Muñoz, P., Navarrete, S. A., Perez, E., Poulin, E., Sellanes, J.,
988 Sepúlveda, H. H., Stotz, W., Tala, F., Thomas, A., Vargas, C. A., Vasquez, J. A. and
989 Vega, J. M. A.: the Humboldt Current System of Northern-Central Chile Oceanographic
990 Processes , Ecological Interactions, edited by R. N. Gibson, R. J. A. Atkinson, and J. D.
991 M. Gordon, Oceanogr. Mar. Biol. An Annu. Rev., 45(3), 195–344, doi:Book_Doi
992 10.1201/9781420050943, 2007.
993
994 Toniazzo, T., Sun, F., Mechoso, C. R. and Hall, A.: A regional modeling study of the
995 diurnal cycle in the lower troposphere in the south-eastern tropical Pacific. Clim. Dyn.,
996 41,1899–1922, doi:10.1007/s00382-012-1598-3, 2013.
997
998 Vazquez-Cuervo, J., Dewitte, B., Chin, T. M., Amstrong, E., Purca, S. and Alburqueque,
999 E.: An analysis of SST gradient off the Peruvian coast; The impact of going to higher
1000 resolution, Remote Sensing of Environment, 131, 76-84, 2013.
1001
1002 Venegas, S.A, Mysak, L.A. and Straub, D.N.: Atmosphere-Ocean Coupled Variability in
1003 the South Atlantic. J. Clim., 10, 2904-2920, 1997.
1004

Webb, E. K.: Profile relationships: The log-linear range, and extension to strong stability. Quart. J. Roy. Meteor. Soc., 96, 67–90, 1970.

Wallace, J., Mitchell, T. and Deser, C.: The influence of sea-surface temperature on surface wind in the eastern equatorial Pacific: Seasonal and interannual variability. J. Climate, 2, 1492–1499, 1989.

Winant, C.D., Dorman, C.E., Friehe, C.A. and Beardsley, R.C.: The marine layer off Northern California: an example of supercritical channel flow. J. Atmos. Sci. 45, 3588–3605, 1988.

Wood, R., Mechoso, C. R., Bretherton, C. S., Weller, R. A., Huebert, B., Straneo, F., Albrecht, B. A., Coe, H., Allen, G., Vaughan, G., Daum, P., Fairall, C., Chand, D., Gallardo Klenner, L., Garreaud, R., Grados, C., Covert, D. S., Bates, T. S., Krejci, R., Russell, L. M., de Szoeke, S., Brewer, A., Yuter, S. E., Springston, S. R., Chaigneau, A., Toniazzo, T., Minnis, P., Palikonda, R., Abel, S. J., Brown, W. O. J., Williams, S., Fochesatto, J., Brioude, J. and Bower, K. N.: The VAMOS Ocean-Cloud-Atmosphere-Land Study Regional Experiment (VOCALS-REx): goals, platforms, and field operations. Atmos. Chem. Phys., 11, 627–654, doi:10.5194/acp-11-627-2011, 2011.

Xie, S.P.: Satellite observations of cool ocean-atmosphere interaction. Bull Amer. Meteor. Soc., 85, 195-208, 2004.

Zhang, D. L., and Anthes, R.A.: A high–resolution model of the planetary boundary layer– sensitivity tests and comparisons with SESAME–79 data. J. Appl. Meteor., 21, 1594–1609, 1982.

1033 **Table 1**: Information of the physics options and main features used in the simulations.

Parameterization	References
Microphysics: WRF Single-Moment 6-class scheme. A scheme with ice, snow and graupel processes suitable for high-resolution simulations.	(Hong et al. 2006)
Longwave/Shortwave radiation: Rapid Radiative Transfer Model (RRTMG). An accurate scheme using look- up tables for efficiency, accounts for multiple bands, trace gases, and microphysics species. It includes the Monte Carlo Independent Column Approximation MCICA method of random cloud overlap.	(Iacono et al. 2008).
Boundary layer: University of Washington Turbulent kinetic energy (TKE) Boundary Layer scheme. This scheme is TKE based, and it is characterized by the use of moist-conserved variables, an explicit entrainment closure, downgradient diffusion of momentum, and con- served scalars within turbulent layers.	(Bretherton and Park 2009)
Surface layer: Based on Monin-Obukhov with Carslon-Boland viscous sub-layer and standard similarity functions from look-up tables.	(Paulson, C. A., 1970) (Dyer, A. J. et al., 1970) (Webb, E. K., 1970) (Beljaars, A.C.M., 1994) (Zhang and Anthes 1982)
Land surface model: The NOAH Land Surface Model. For land surface processes including vegetation, soil, snowpack and land atmosphere energy, momentum and moisture exchange.	(Tewari, M. et al., 2004)
Cumulus: Betts-Miller-Janjic scheme. Operational Eta scheme. Column moist adjustment scheme relaxing towards a well-mixed profile.	(Janjic, Z. I., 2000)

1034

FIGURE CAPTIONS

Figure 1. Study area showing bathymetry and topography of the coastal terrain. The dotted thick line indicates the western boundary of the coastal band where satellite information (~25 km offshore) is absent. Red squares indicate the location of the three weather stations at Loma de Hueso, Punta Lengua de Vaca and Parral Viejo. The inset plot shows the three model domains used in the WRF simulations (36, 12 and 4 km).

Figure 2. Comparisons of the spatial patterns of the mean velocity fields of winds obtained (common period 2007-2009) from a) QuikSCAT b) WRF simulation for the 36 km grid configuration. c) Root Mean Square (RMS) differences between observations and model results. The lower panels show dispersion plots between the observed and modeled N-S winds at d) Loma de Hueso, e) Parral Viejo and f) Punta Lengua de Vaca (Fig.1). Red line represent to linear regress and black line is 1:1 relation.

Figure 3. Mean wind stress curl obtained by the model (for 2007-2012) using three model domains a) 36 km, b) 12 km and c) 4 km. The yellow dotted line represents the length scale of the wind drop-off determined from a threshold value of -0.3×10^{-4} s^{-1} (Renault et al., 2015). d) Mean zonal profiles of alongshore wind speed obtained from the three model configurations (36, 12 and 4 km) and QuikSCAT observations are shown. e) Zonal profiles of alongshore wind speed from a weather station obtained onboard of a fishing boat during 22 April (black line), 18 May (black dashed line), 15 September (red line) and 28 October (red dashed line) of 2014 are also shown. The segmented line in d) and e) indicates the location of the satellite blind spot.

Figure 4. Wind stress annual cycle obtained from the simulation at 4 km resolution (for 2007-2012). Color represents the magnitude of wind stress (in Nm^{-2}) and the arrows indicate the wind stress direction.

Figure 5. Annual cycle of Ekman pumping (vertical velocity in md^{-1}) obtained from the simulation at 4 km resolution (for 2007-2012).

Figure 6. Hovmoller diagrams of alongshore wind stress seasonal cycle (top panels) and the zonal gradient of alongshore wind (lower panels) for the regions at 28.5ºS (a, d), 30.5ºS (b, e) y 32.5ºS (c, f). The monthly mean zonal wind stress and mean zonal gradient are also shown (side black line).

Figure 7. Contributions of the coastal divergence (CD) and Ekman pumping (EP) to the vertical transport near the coast. a) Integrated orography index (H_{index}, black line) and coastaline meander index (M_{index}, red line, see text). b) Drop-off spatial length. c) Alongshore wind at Ld (red line) and coastal (black line). d) Ratio between Ekman pumping and coastal divergence. e) Seasonal vertical transport associated with coastal divergence and f) seasonal vertical transport associated with Ekman pumping. To estimate the coastal divergence the wind stress closest to the coast was used, while Ekman pumping was integrated from the coast to the longitude corresponding to a distance from the coast equal to the length of the drop-off (see text).

Figure 8. Contributions of coastal divergence (CD) and Ekman pumping (EP) to the vertical transport near the coast (in Sv) over the study area (27.75°S-32.5°S, see Fig. 7). Seasonal vertical transport associated with coastal divergence (black line), Ekman pumping (red line) and total wind induced vertical transport (blue line, sum of both vertical transports). The estimates were carried out from the WRF simulation at 4 km resolution.

Figure 9. Annual cycle of sea surface temperature obtained using data from the Multi-scale Ultra-high Resolution (MUR). Top and bottom panels used a different colormap scale.

Figure 10. October mean spatial distribution for a) wind stress and b) Ekman pumping using the 4 km grid spacing simulation and c) sea surface temperature (SST) and d) SST gradient obtained from MUR observations.

1096 Figure 11. First SVD mode between Ekman pumping (WEk) from the WRF simulation at
1097 4 km resolution and sea surface temperature (SST) from MUR data. a) The Ekman
1098 pumping spatial component. b) The SST spatial component. c) The black (red) line
1099 represents the associated Ekman pumping (SST) time series. Note that the units are
1100 arbitrary.

FIGURES

Figure 1.

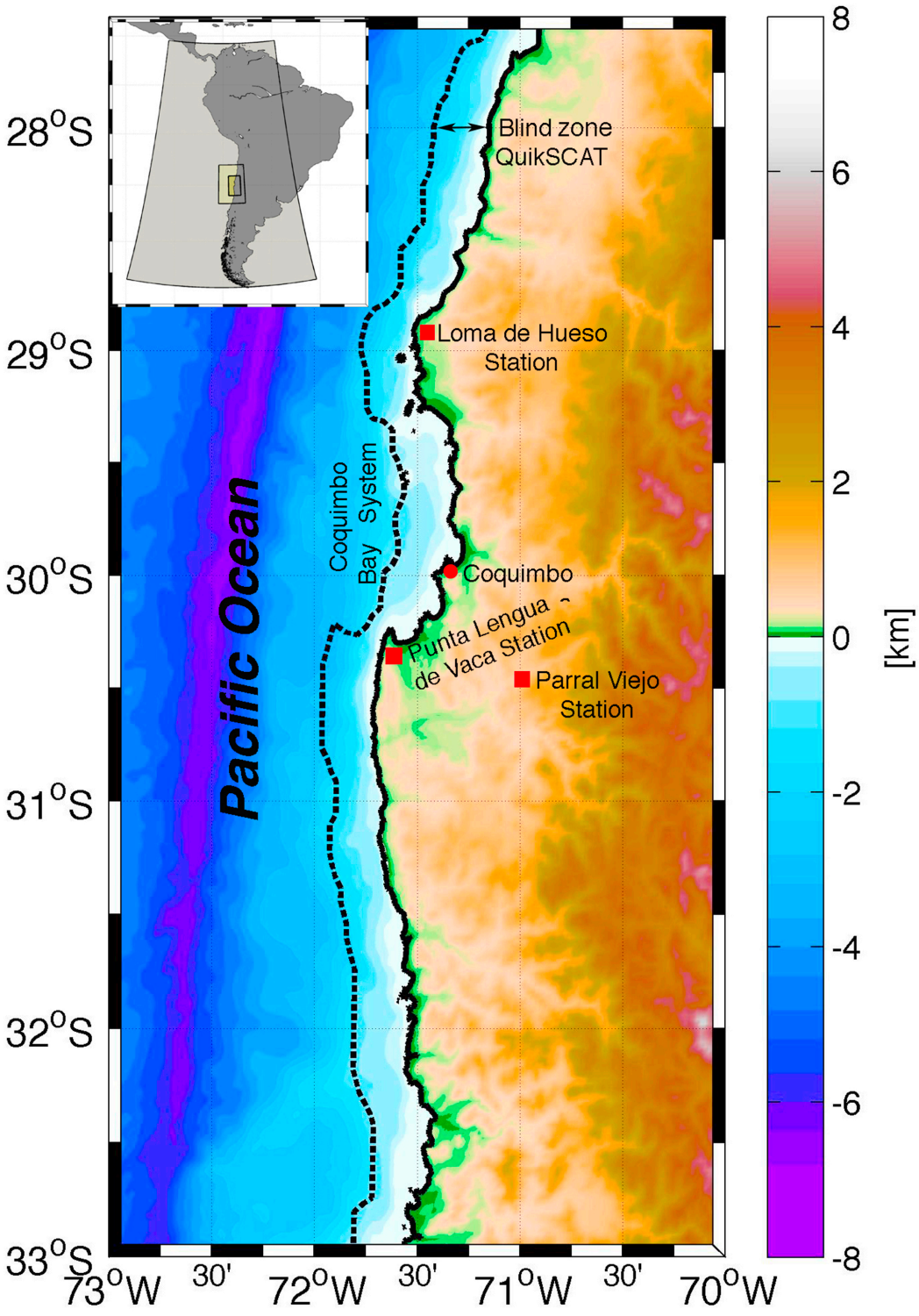

Figure 2.

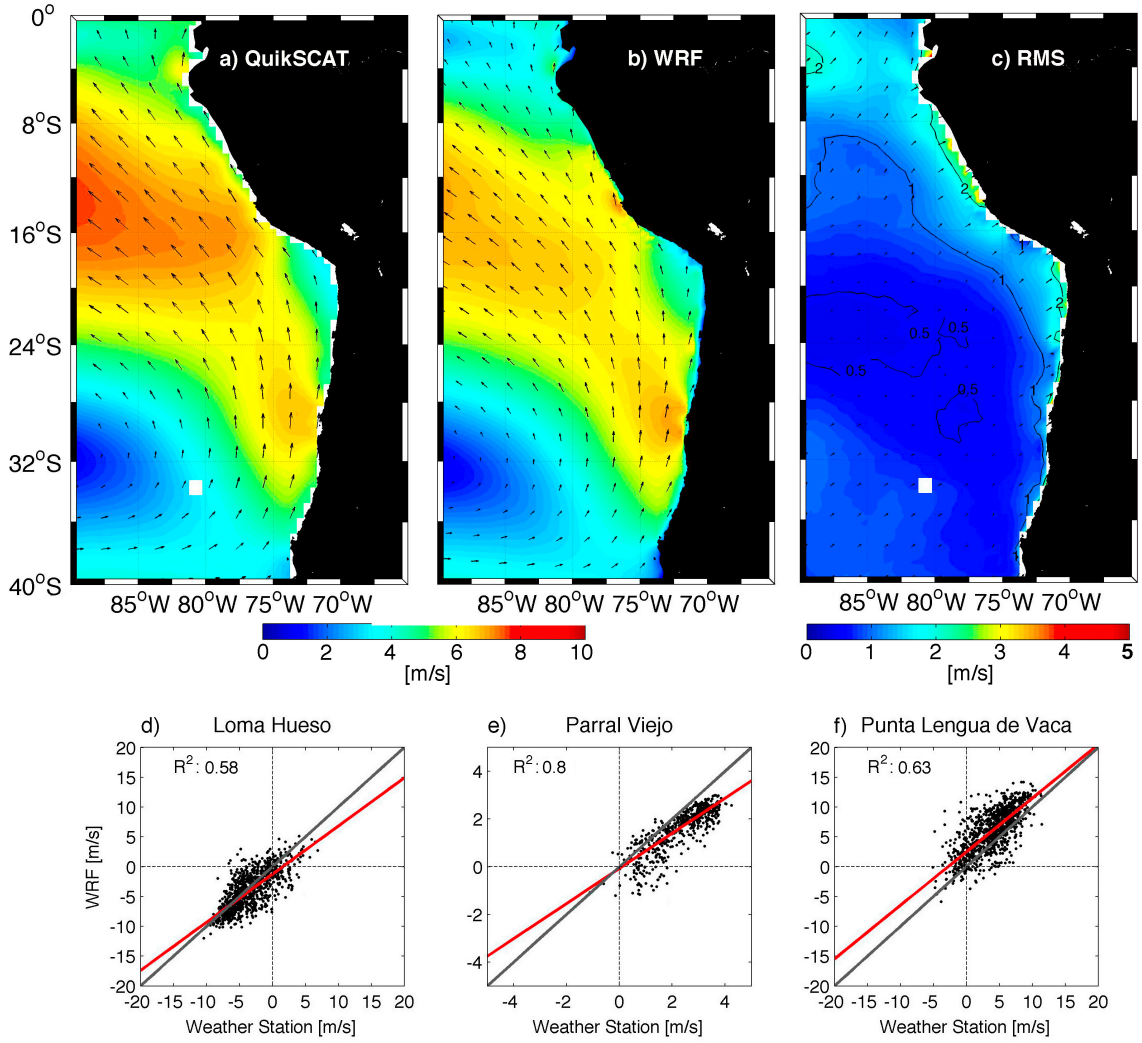
a) QuikSCAT
b) WRF
c) RMS
0°
8°S
16°S
24°S
32°S
40°S
85°W 80°W 75°W 70°W
0 2 4 6 8 10
[m/s]
0 1 2 3 4 5
[m/s]
d) Loma Hueso
R²: 0.58
e) Parral Viejo
R²: 0.8
f) Punta Lengua de Vaca
R²: 0.63
WRF [m/s]
Weather Station [m/s]

Figure 3.

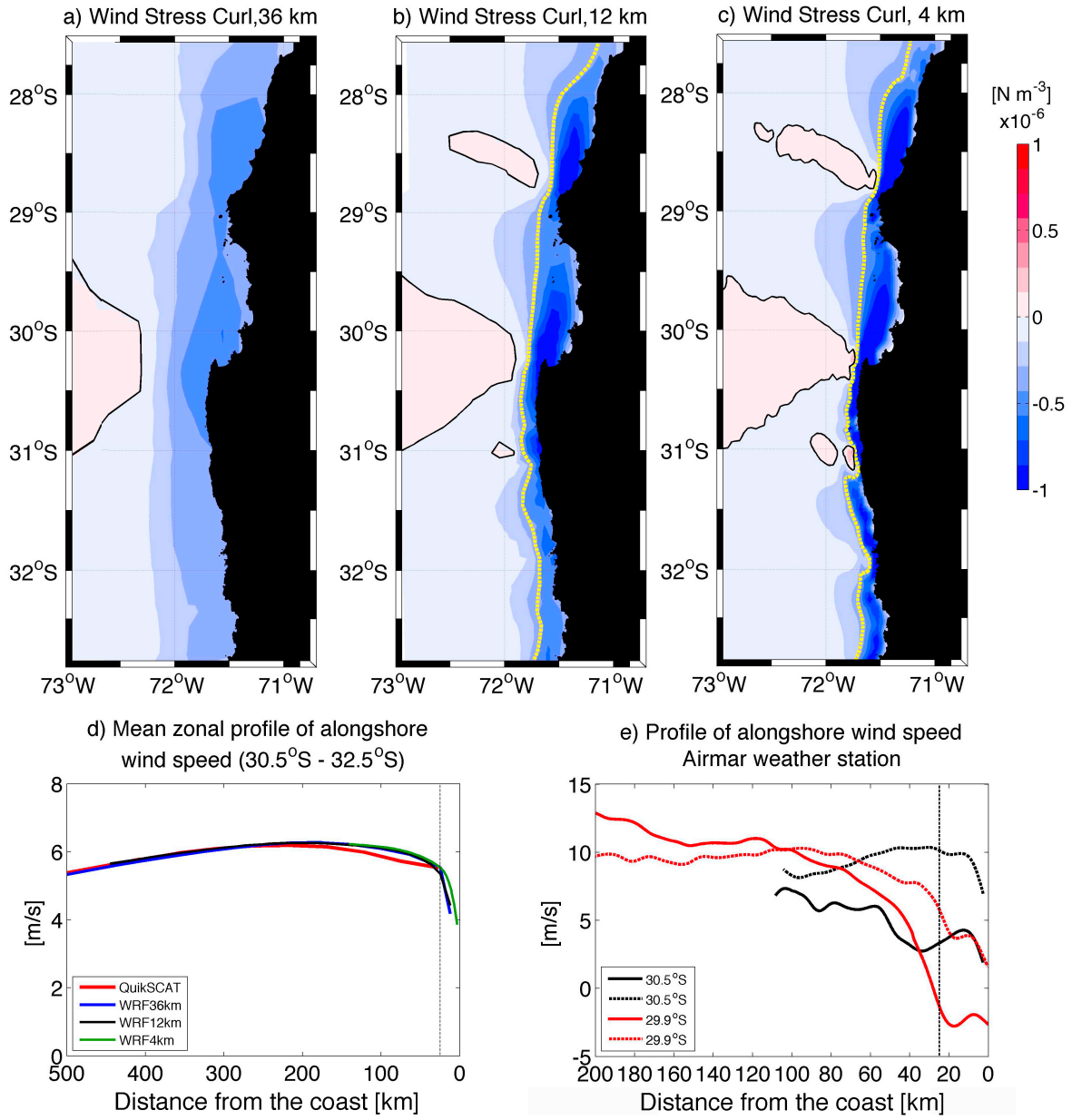
a) Wind Stress Curl,36 km
b) Wind Stress Curl,12 km
c) Wind Stress Curl, 4 km
28°S
29°S
30°S
31°S
32°S
73°W
72°W
71°W
[N m-3]
x10-6
1
0.5
0
-0.5
-1
d) Mean zonal profile of alongshore wind speed (30.5°S - 32.5°S)
[m/s]
QuikSCAT
WRF36km
WRF12km
WRF4km
Distance from the coast [km]
e) Profile of alongshore wind speed Airmar weather station
30.5°S
30.5°S
29.9°S
29.9°S
Distance from the coast [km]

Figure 4.

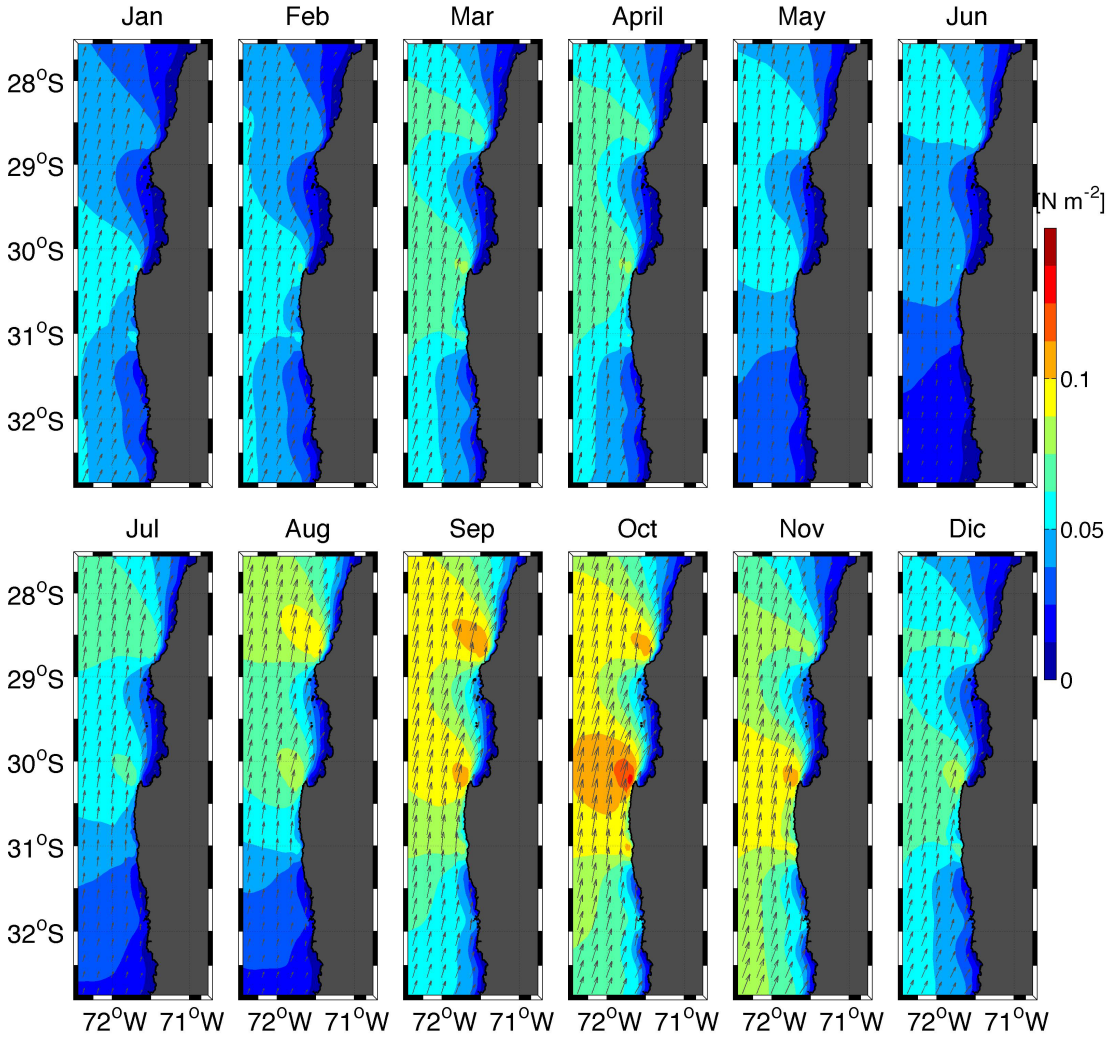
Jan
Feb
Mar
April
May
Jun
Jul
Aug
Sep
Oct
Nov
Dic
28°S
29°S
30°S
31°S
32°S
72°W 71°W
[N m-2]
0.1
0.05
0

Figure 5.

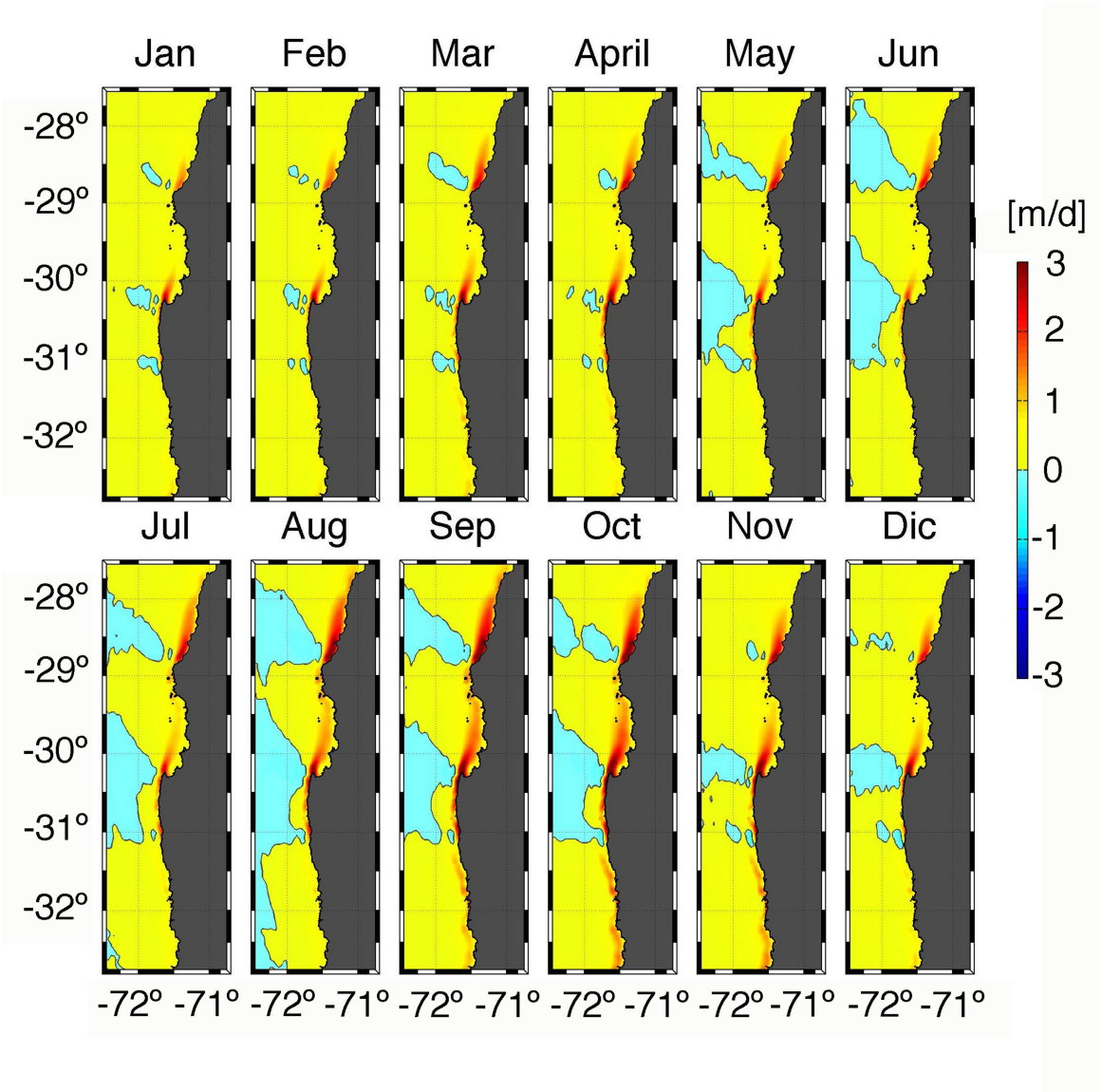
Jan
Feb
Mar
April
May
Jun
Jul
Aug
Sep
Oct
Nov
Dic
-28°
-29°
-30°
-31°
-32°
-72° -71°
[m/d]
3
2
1
0
-1
-2
-3

Figure 6.

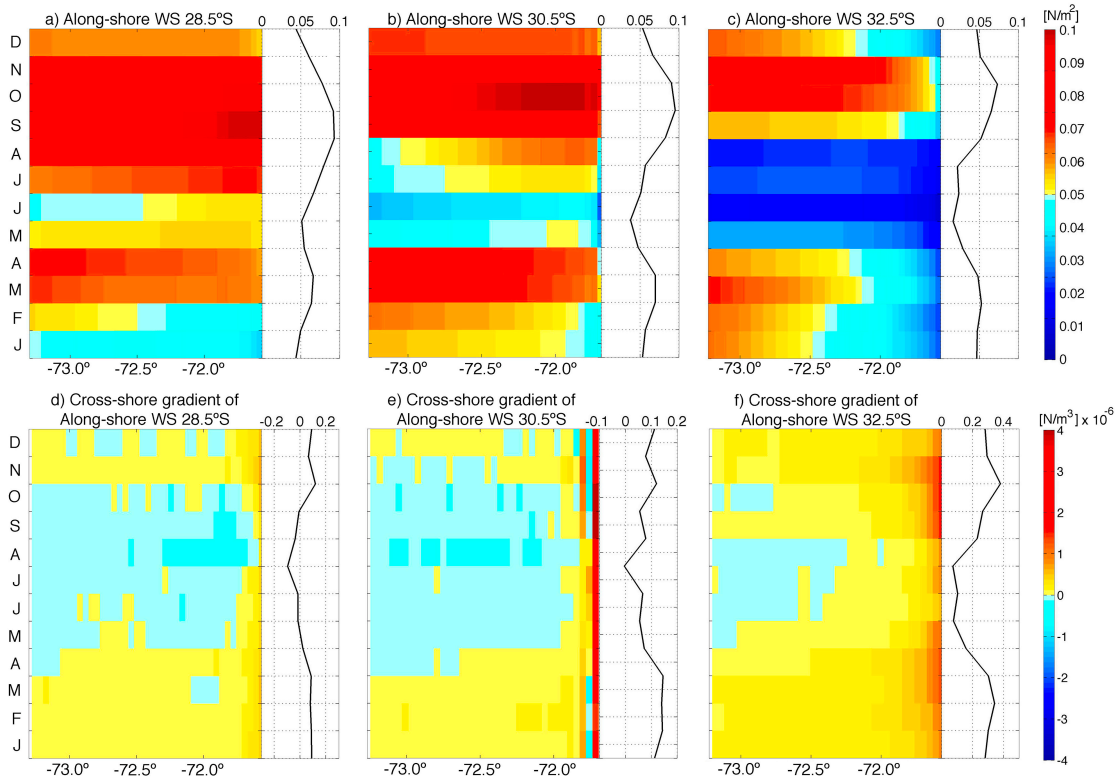
a) Along-shore WS 28.5ºS
b) Along-shore WS 30.5ºS
c) Along-shore WS 32.5ºS
d) Cross-shore gradient of Along-shore WS 28.5ºS
e) Cross-shore gradient of Along-shore WS 30.5ºS
f) Cross-shore gradient of Along-shore WS 32.5ºS
D
N
O
S
A
J
J
M
A
M
F
J
-73.0º
-72.5º
-72.0º
[N/m2]
[N/m3] x 10-6

Figure 7.

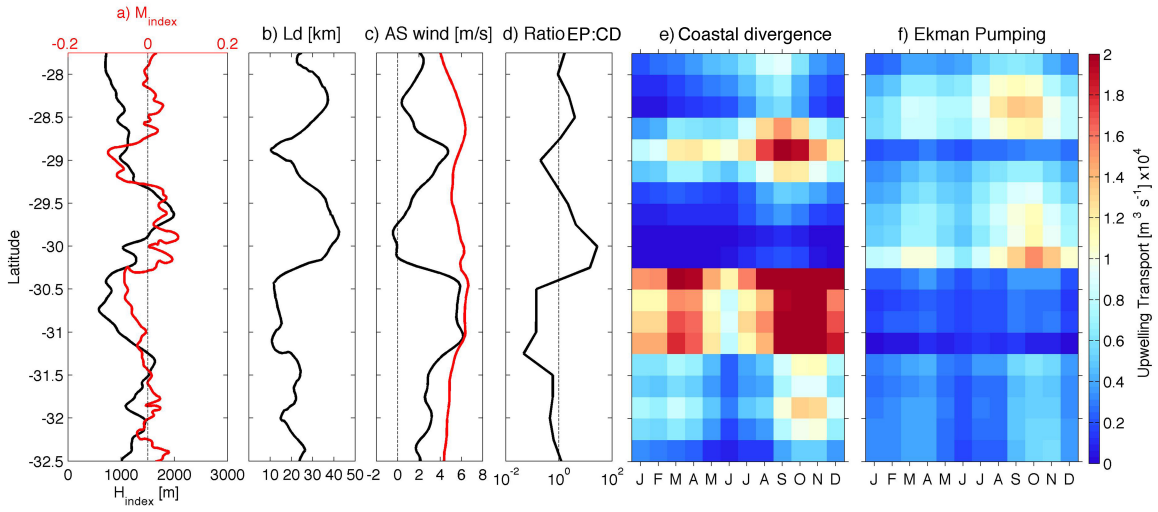
a) M index
-0.2
0
0.2
b) Ld [km]
c) AS wind [m/s]
d) Ratio EP:CD
e) Coastal divergence
f) Ekman Pumping
Latitude
-28
-28.5
-29
-29.5
-30
-30.5
-31
-31.5
-32
-32.5
0
1000
2000
3000
H index [m]
10 20 30 40 50
-2 0 2 4 6 8
10-2
100
102
J F M A M J J A S O N D
J F M A M J J A S O N D
2
1.8
1.6
1.4
1.2
1
0.8
0.6
0.4
0.2
0
Upwelling Transport [m 3 s -1] x10 4

Figure 8.

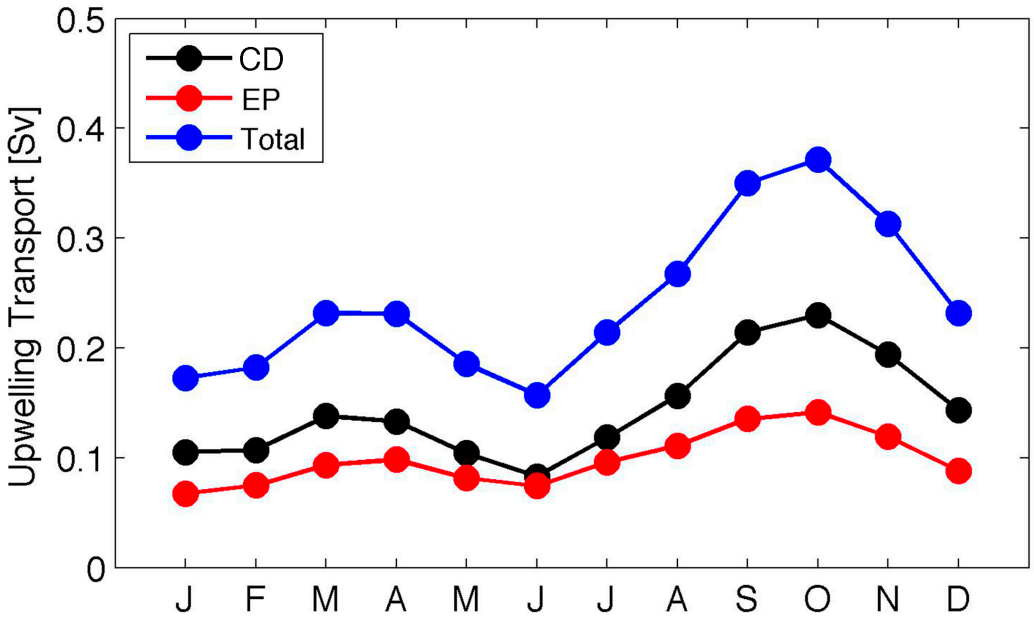
0.5
0.4
0.3
0.2
0.1
0
Upwelling Transport [Sv]
CD
EP
Total
J
F
M
A
M
J
J
A
S
O
N
D

Figure 9.

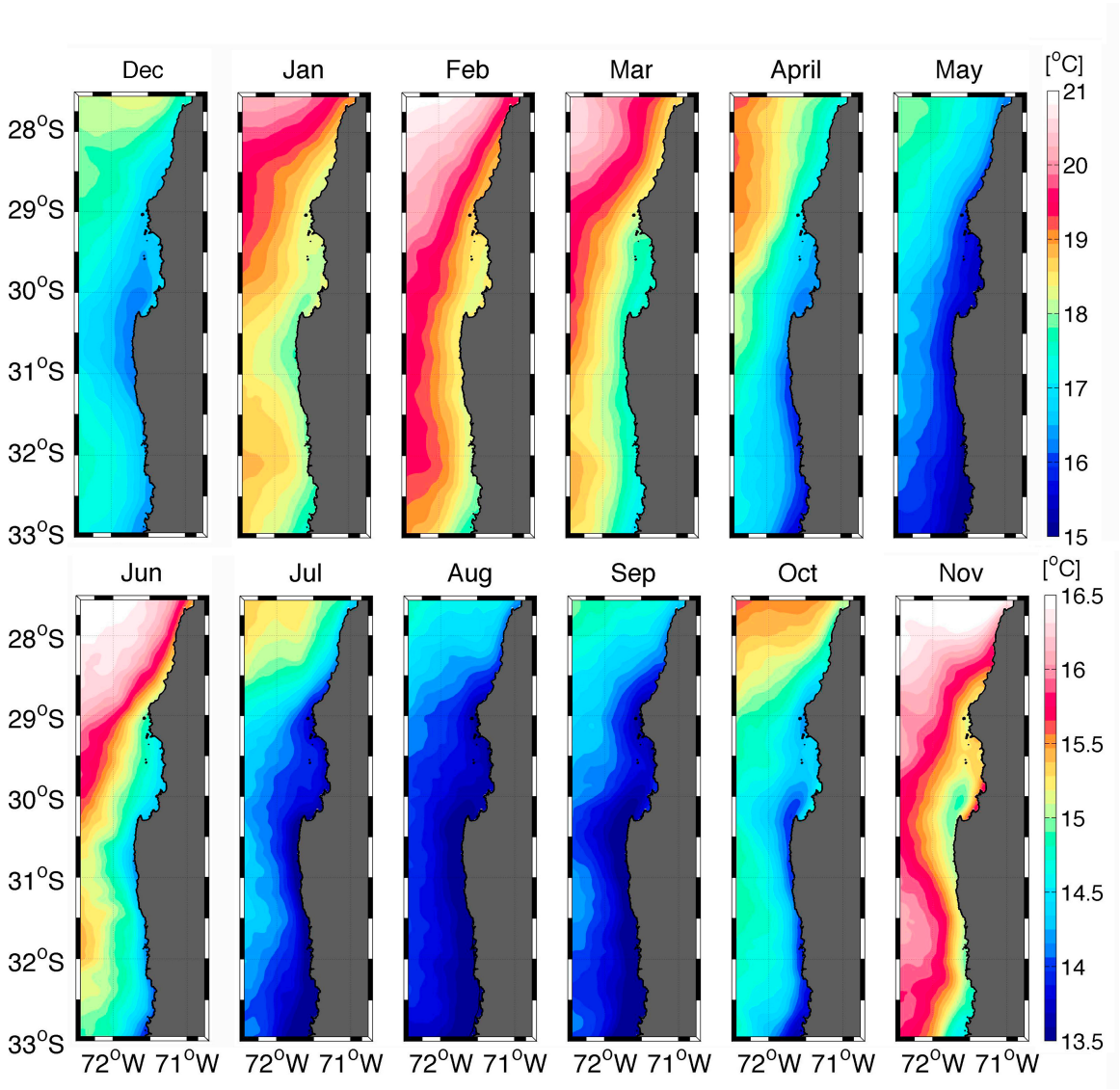
Dec
Jan
Feb
Mar
April
May
[°C]
21
20
19
18
17
16
15
28°S
29°S
30°S
31°S
32°S
33°S
Jun
Jul
Aug
Sep
Oct
Nov
[°C]
16.5
16
15.5
15
14.5
14
13.5
72°W 71°W

Figure 10.

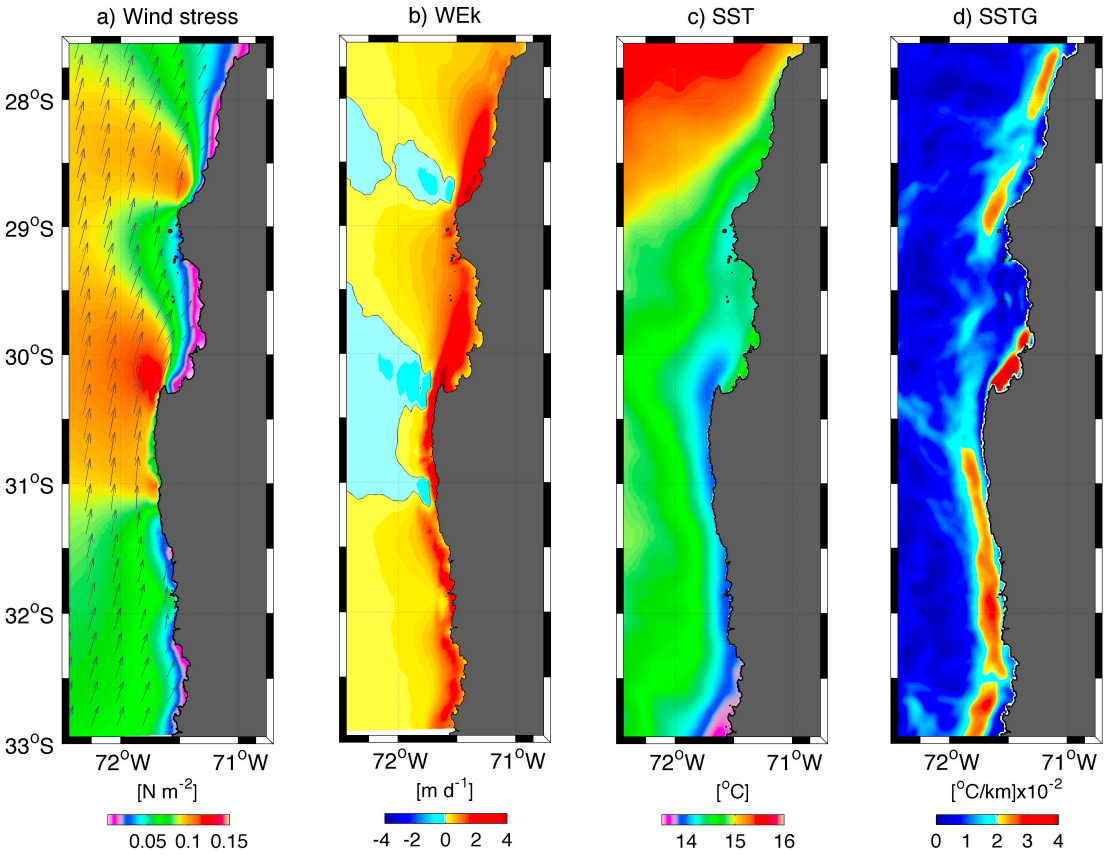
a) Wind stress
b) WEk
c) SST
d) SSTG
28°S
29°S
30°S
31°S
32°S
33°S
72°W
71°W
[N m-2]
0.05 0.1 0.15
[m d-1]
-4 -2 0 2 4
[°C]
14 15 16
[°C/km]x10-2
0 1 2 3 4

Figure 11.

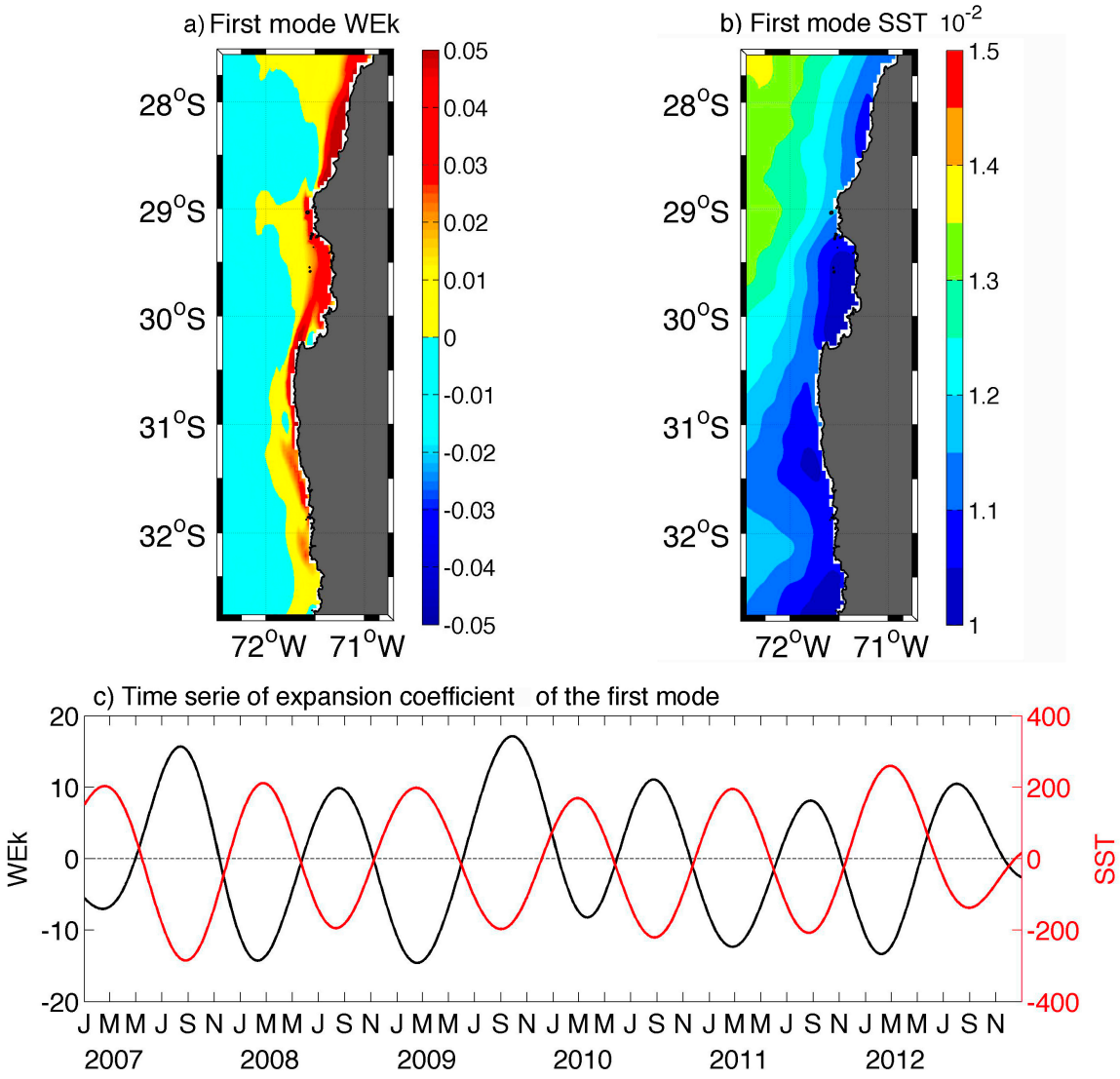
a) First mode WEk
28°S
29°S
30°S
31°S
32°S
72°W
71°W
0.05
0.04
0.03
0.02
0.01
0
-0.01
-0.02
-0.03
-0.04
-0.05
b) First mode SST 10-2
1.5
1.4
1.3
1.2
1.1
1
c) Time serie of expansion coefficient of the first mode
WEk
SST
20
10
0
-10
-20
400
200
0
-200
-400
J M M J S N J M M J S N J M M J S N J M M J S N J M M J S N J M M J S N
2007
2008
2009
2010
2011
2012